J. Fluid Mech. (2000), *vol.* 418, *pp.* 231–264. Printed in the United Kingdom

Prediction and investigation of the turbulent flow over a rotating disk

By XIAOHUA WU† AND KYLE D. SQUIRES

Mechanical and Aerospace Engineering Department, Arizona State University, Box 876106, Tempe, AZ 85287-6106, USA

(Received 20 July 1998 and in revised form 25 April 2000)

Large-eddy simulation (LES) has been used to predict the statistically three-dimensional turbulent boundary layer (3DTBL) over a rotating disk. LES predictions for six parameter cases were compared to the experimental measurements of Littell & Eaton (1994), obtained at a momentum thickness Reynolds number of 2660. A signal-decomposition scheme was developed by modifying the method of Spalart (1988) to prescribe time-dependent boundary conditions along the radial direction, entrainment towards the disk surface was prescribed by satisfying global mass conservation. Predictions of the mean velocities and r.m.s. fluctuations are in good agreement with data, with the largest discrepancy occurring in the prediction of the wall-normal intensities. The primary and two secondary shear stresses are also in good agreement with the measurements and one-dimensional energy spectra of the velocity fluctuations agree well with established laws, i.e. a -1 slope in the buffer region and $-5/3$ slope near the edge of the boundary layer.

Conditionally averaged velocities provide new evidence in support of the structural model of Littell & Eaton (1994) concerning the interaction of mean-flow three-dimensionality and shear-stress producing structures. Inside the buffer region under strong ejections, the conditionally averaged crossflow (radial) velocity is larger than the unconditioned mean, and the profile conditioned on strong sweeps is smaller than the mean. This is consistent with the notion that streamwise vortices having the same sign as the mean streamwise vorticity, and beneath the peak crossflow location, are mostly responsible for strong sweep events; streamwise vortices with opposite sign as the mean streamwise vorticity promote strong ejections. Comparison of two-point spatial correlations with previous measurements in two-dimensional turbulent boundary layers (2DTBLs) indicates interesting structural similarities, e.g. the correlation of wall pressure and surface-normal velocity fluctuations is an odd function of streamwise separation, being positive downstream and negative upstream. These similarities offer quantitative indirect support to the hypothesis advanced by Littell & Eaton (1994) and Johnston & Flack (1996) that structural models describing 2DTBLs may be employed as a baseline in (equilibrium) 3DTBL structural studies.

1. Introduction

1.1. *Overview and objectives*

Consider the flow over a flat disk which rotates about an axis, z, perpendicular to its plane with a uniform angular velocity, ω, in an otherwise stationary incompressible

† Present address: Center for Integrated Turbulence Simulations, Stanford University, Building 500, Stanford, California, USA.

fluid that fills the entire half-space, $z \geqslant 0$. The layer near the disk is carried by it through friction and is thrown outward owing to the action of centrifugal forces. As illustrated in figure 1(*a*), this is compensated by particles which flow in an axial direction towards the disk to be in turn carried and ejected centrifugally (Schlichting 1979). Inside the layer, all three velocity components u_r, u_θ, and u_z and their mean are non-zero. As discussed in Kobayashi (1994), the flow over a rotating disk is laminar for Reynolds numbers $Re = \omega r^2/\nu$ less than about 4.5×10^4, where r is the radial coordinate and ν the kinematic viscosity. The flow is fully turbulent for Re greater than about 3.9×10^5. Lingwood (1996) pointed out that the onset of transition over a rotating disk occurs at $Re_{\delta_2} = (\omega r)\delta_2/\nu$ above 502 and below 513, where δ_2 is the boundary-layer momentum thickness. The tangential velocity distribution resembles a fully turbulent profile by $Re_{\delta_2} = 615$.

The boundary layer induced by a rotating disk in an otherwise quiescent fluid bears substantial scientific importance owing to its relevance to applications in electronic packaging and turbomachinery, among others. It is also a flow of fundamental interest for several reasons. The laminar flow is one of the few non-trivial three-dimensional cases whose exact Navier–Stokes solutions exist. The solution to the laminar flow over a rotating disk was first discussed by von Kármán, and subsequently followed by many others (see Schlichting 1979). In these studies, the assumption that similarity solutions to the velocity components exist is invoked. Transformations similar to those used for axisymmetric stagnation point flow are then used to reduce the Navier–Stokes equations to a pair of ordinary differential equations (e.g. see Schlichting 1979). The transitional flow over a rotating disk affords a unique three-dimensional platform for the investigation of instability and turbulence origin. The stability of the laminar boundary layer over a rotating disk and the related transition problem has been extensively considered by Malik, Wilkinson & Orszag (1981); Balachandar, Streett & Malik (1992); and Lingwood (1996, 1997), among others. Transition over a rotating disk, while of significant interest and importance, is not the subject of this paper and the reader is referred to the work of the aforementioned authors, and in particular to Kobayashi (1994) and Lingwood (1997) for recent reviews. Likewise, the confined flow between co-rotating disks, which also has wide applications, is beyond the scope of the present investigation. The reader is referred to the work of Humphrey & Gor (1993) for discussions on that subject.

Compared to the laminar and transitional flows, the fully turbulent three-dimensional boundary layer over a rotating disk has been the subject of considerably fewer investigations. Unlike three-dimensional turbulent boundary layers (3DTBLs) which are formed by turning, via a spanwise pressure gradient or shearing force, an initially two-dimensional turbulent flow, the disk boundary layer is unique in that it is three-dimensional from its inception. Consequently, the underlying structure does not result from perturbing an initially two-dimensional flow, but is inherent to a boundary layer with a continuously applied crossflow. The rotating disk boundary layer is then one of the most canonical platforms for investigation of the underlying structure of 3DTBLs. Increased knowledge and an improved understanding of the disk boundary-layer structure establishes an important basis for understanding other 3DTBLs arising in more complex configurations.

As described in greater detail in § 1.2, the most thorough experimental investigation of the statistical and structural features of the 3DTBL over a rotating disk is that conducted by Littell & Eaton (1994). A key feature of their study concerned modification of boundary-layer turbulence by the crossflow. Littell & Eaton (1994) first hypothesized that a plausible description of the equilibrium structure of the

disk flow turbulence is a modification of the baseline structural model advanced by Robinson (1991) for two-dimensional boundary layers. Based upon measurements obtained using conditional sampling and two-point correlations, Littell & Eaton (1994) then proposed a model accounting for modification of boundary-layer structure by the crossflow (see also Eaton 1995). One of the main goals of the present work is to scrutinize more closely the proposed structural model and associated hypothesis advanced by Littell & Eaton (1994) and, in general, to provide a more developed understanding of the similarities and differences between a well-defined, equilibrium 3DTBL over a rotating disk and canonical two-dimensional turbulent flows which have been more widely studied. One of the main contributions of this study is that the structural model proposed by Littell & Eaton (1994) has been validated using new, definitive measures of the near-wall structure, and their working hypothesis has also been indirectly reinforced using insight gained from new measurements of two-point spatial correlations.

The approach adopted in this work for investigation of the 3DTBL over a rotating disk is large-eddy simulation (LES). As described in § 2, LES is used to resolve boundary-layer turbulence in a Reynolds number range for which measurements exist, outside the range at which a direct simulation could be considered feasible. While LES permits an accurate description of the disk flow, a time-dependent and three-dimensional simulation poses significant new challenges, and calculations of the disk boundary layer must be carefully constructed and performed. In LES, a subgrid model is employed to parameterize stresses not resolved by the computational grid. The additional empiricism introduced by the subgrid model must be carefully considered before the results from an LES calculation may be used to gain insight into fundamental aspects of the flow. In addition, a reasonably large body of literature now exists concerning application of LES to prediction of complex turbulent flows and it is clear that comparison to experimental measurements is crucial in order to validate the entire computational approach.

The two primary aims of this work are (i) prediction of the 3DTBL over a rotating disk using LES, and (ii) investigation of the underlying structure of the flow. The data of Littell & Eaton (1994) acquired at a momentum thickness Reynolds number 2660 are used to evaluate LES predictions. In § 1.2 a survey of previous work on the fully turbulent flow over a rotating disk is presented. Some related studies on other 3DTBLs are also discussed in § 1.2. A summary of recent applications of LES to prediction of complex flows is presented in § 1.3.

1.2. *Three-dimensional turbulent boundary layers*

Cham & Head (1969) measured the mean tangential velocity $\langle u_\theta \rangle$ and mean radial velocity $\langle u_r \rangle$ (cf. figure 1) in the 3DTBL over a rotating disk for $3.0 \times 10^5 \leqslant Re \leqslant 2.0 \times 10^6$. In addition to the mean tangential and radial velocities, Erian & Tong (1971) also measured two turbulence intensities $u'_{\theta,rms}$ and $u'_{r,rms}$, as well as the primary turbulent shear stress $\langle u'_\theta u'_z \rangle$ for $6.0 \times 10^5 \leqslant Re \leqslant 1.0 \times 10^6$. More recently, Littell & Eaton (1994) reported a comprehensive experimental study in the range $4.0 \times 10^5 \leqslant Re \leqslant 1.6 \times 10^6$. Their measurements include the mean velocity components and all six Reynolds stresses. Littell & Eaton (1994) also measured two-point correlations and used conditional sampling away from the wall ($z^+ > 100$) to investigate modification by the crossflow of the production of turbulent shear stress. Similar two-point correlation measurements were recently presented by Kang, Choi & Yoo (1998). Computational work on the disk boundary layer is scarce. Cham & Head (1969), Copper (1971), and Cebeci & Abbott (1975) calculated the mean velocity

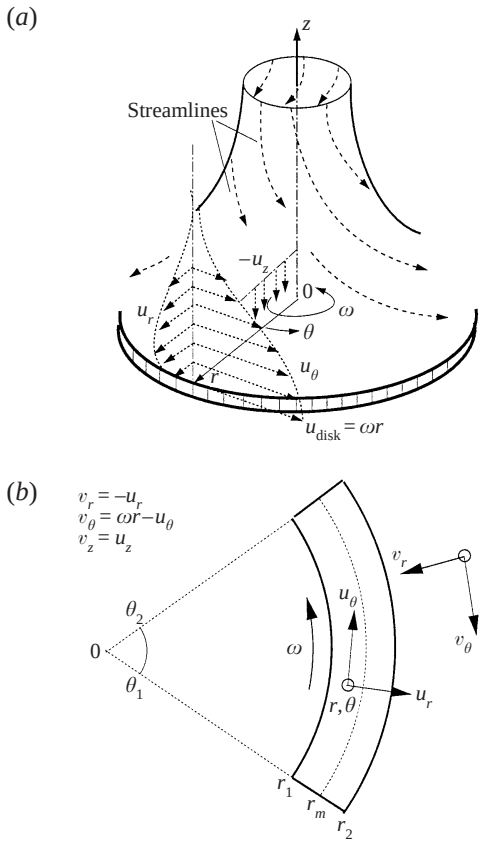

FIGURE 1. (*a*) Schematic of the 3DTBL created over a rotating disk in the laboratory coordinate system; (*b*) top-view of the computational domain.

components $\langle u_\theta \rangle$ and $\langle u_r \rangle$ using the laminar similarity method of von Kármán and empirical eddy viscosities.

Experimental studies and direct numerical simulations of 3DTBLs up to 1996 were reviewed by Johnston & Flack (1996) (see also Anderson & Eaton 1989; Spalart 1989; Moin *et al.* 1990; Coleman, Ferziger & Spalart 1990; Sendstad & Moin 1992; Schwarz & Bradshaw 1994; Simpson & Olcmen 1995). More recent 3DTBL studies were reported by Coleman *et al.* (1996), Webster *et al.* (1996), and Wu & Squires (1997). Previous work indicates that understanding and prediction has been hampered by the many complicating features such as upstream flow development, streamwise pressure gradient, and surface curvature that are often present in the majority of 3DTBLs. Webster *et al.* (1996) found that in the flow over a swept bump, effects of mean-flow three-dimensionality on boundary-layer properties were less significant than changes caused by the streamwise pressure gradient. The stress/intensity ratio, for example, was nearly the same as in its two-dimensional analogue. Their findings are consistent with the direct simulations performed by Coleman *et al.* (1996) of turbulent channel flow subjected to additional mean strains. Coleman *et al.* (1996) found a stronger effect of the strains resulting from streamwise pressure gradient on structural descriptors of the turbulence as compared to the effect of mean-flow three-dimensionality.

Compared to other 3DTBLs, the fully turbulent flow over a rotating disk is unique

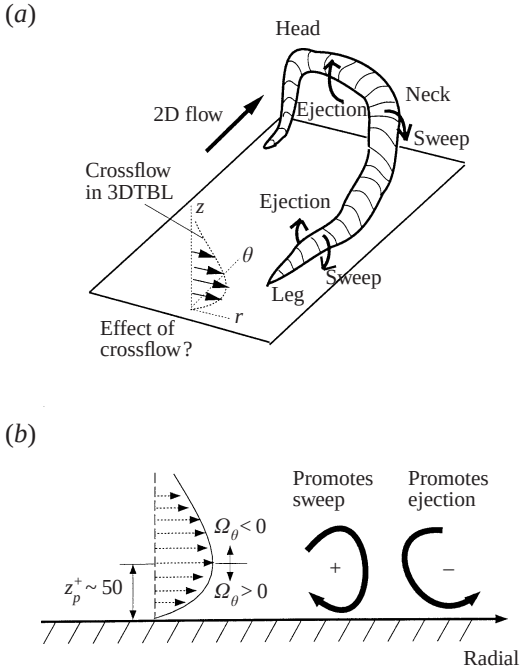

FIGURE 2. (*a*) Schematic of the canonical 2DTBL structure model of Robinson (1991) and the crossflow profile in the disk boundary layer; (*b*) Littell & Eaton (1994) model of alteration of shear-stress producing events by the mean crossflow (see also Eaton 1995).

since there are no other complicating effects arising from variations in geometry, streamwise pressure gradient, etc. Successful prediction of the disk flow then establishes an important baseline for methods used to predict other complex flows. In addition, a simulation database may be used to study and understand, in a canonical setting, the effect of mean-flow three-dimensionality on boundary-layer turbulence. In fact, noting that few turbulence simulations are available of the disk flow, Johnston & Flack (1996) concluded their review by 'urging modellers to tackle this case as a prelude to the prediction of more complex flows'. The first objective of the current contribution is to apply LES to prediction of the 3DTBL over a rotating disk and evaluate simulation results using the measurements of Littell & Eaton (1994).

The central flow physics question considered in detail by Littell & Eaton (1994) is the modification of shear-stress producing structures by the crossflow. By assuming that the underlying structure of an equilibrium 3DTBL is not fundamentally different from its two-dimensional counterpart, Littell & Eaton first hypothesized that the model of Robinson (1991) developed for two-dimensional boundary layers can be used as an approximation to the shear-stress producing structure in their 3DTBL. In Robinson's model, most ejections are found on the upstream side of transverse vortices, which often form 'head' elements of one- or two-sided vortical arches; strong sweeps occur primarily on the outboard side of tilted necks (see figure 2*a*). Using this baseline model, Littell & Eaton (1994) then proposed that the modification of shear-stress producing structure by mean-flow three-dimensionality can be described as follows: the crossflow reduces the ability of streamwise vortices of one sign to produce strong ejections, while weakening the ability of those of the other sign to produce strong sweeps (see figure 2*b*). In support of their proposition, Littell &

Eaton (1994) showed that conditionally sampled wall-normal velocities at $z^+ > 100$, a position above the location of the peak crossflow, exhibited an asymmetry on the upstream and downstream side (in the radial direction) of ejection/sweep events (see Eaton 1995; Wu & Squires 1997 for further discussions). While this proposition represents a significant step forward in the understanding of 3DTBL structure, a direct test of their model requires examination of the radial velocity profiles beneath the peak of the mean crossflow and conditionally averaged on strong ejections and sweeps (see § 4.2.1 for further details).

An additional issue related to the proposition of Littell & Eaton (1994) is that the structural model of Robinson (1991) developed for canonical two-dimensional boundary layers was employed as the baseline for the disk flow. In order to establish this proposition on firmer ground, it is necessary to understand more deeply the overall structural similarities between the disk boundary layer and the more widely studied two-dimensional turbulent flows, i.e. to clarify whether structural models developed for the latter can indeed be used as a baseline for the former. A definitive clarification of this issue beyond reasonable doubt is difficult. One approach to providing quantitative support for their hypothesis is measurement of two-point correlation functions. If the flow truly contains a dominant structure, distributed stochastically in space, its presence should be clearly marked by two-point correlations (Moin & Kim 1985). Therefore, conditional sampling and two-point spatial correlation measurements are used to achieve the second objective, i.e. to provide a direct evaluation of the structural model of Littell & Eaton (1994), and also to provide some indirect, but quantitative, results concerning their structural similarity hypothesis.

1.3. *Prediction of complex flows using LES*

In this work, LES of the incompressible Navier–Stokes equations is employed. As shown in detail in § 2, filtering the momentum equations yields the subgrid-scale (SGS) stress, which in this study is parameterized using dynamic models. Previous studies in LES and dynamic modelling up to 1996 were reviewed by Lesieur & Metais (1996). Among the more recent investigations are those reported by Rodi *et al.* (1997), Mittal & Moin (1997), Kravchenko & Moin (1997), and Vreman, Guerts & Kuerten (1997). An important outcome of these and other studies is that there are many factors affecting the accuracy of LES predictions, e.g. grid resolution and distribution, subgrid model, numerical methods, and boundary conditions, each of which must be carefully monitored and controlled.

Rodi *et al.* (1997) surveyed the status of LES research through comparison of experimental measurements of the flow past a square cylinder to the simulation results obtained by ten groups. LES predictions obtained using wall-layer models produced drag coefficients that were relatively closer to experimental measurements, while calculations resolving the wall layer (i.e. directly enforcing no-slip conditions) tended to yield higher values of the drag coefficient. Simulations using dynamic models tended to predict longer recirculation zones and lower drag coefficients, and in better agreement with measurements, than in calculations performed using the Smagorinsky model. Accurate prediction of some global parameters such as the Strouhal number did not necessarily indicate a quality simulation. Rodi *et al.* (1997) concluded that one of the keys to accurate predictions is having sufficient resolution near the wall, whether no-slip boundary conditions or wall-layer models are used. Insufficient spanwise resolution and inadequate spanwise dimensions were also possible contributors to the lack of agreement with experiments. Rodi *et al.* (1997) pointed out that one of the factors whose effect proved difficult to analyse was

the choice of numerical method. Upwind methods, for example, have a dissipative truncation error that can act as an additional subgrid model. For the flow around a square cylinder, numerical schemes using upwind methods tended to predict short recirculation zones owing to the numerical diffusion added by the discretization.

Mittal & Moin (1997) studied the effect of numerical discretization through comparison of LES predictions of the flow past a circular cylinder using a conservative second-order central difference method to higher-order upwind-biased schemes. The upwind-biased schemes removed excessive energy from roughly three-quarters of the resolved wavenumber range owing to inherent numerical dissipation. In the central difference scheme, because there is no numerical dissipation, the smaller scales were more energetic and the computed energy spectra agreed better with experiments. With about twenty per cent smaller grid spacing, the second-order method yielded mean flow and Reynolds stress results that are comparable to those obtained by the high-order upwind schemes. Based on these results, Mittal & Moin (1997) advocated that in applications such as flow-generated noise and reacting flows where small-scale fluctuations play a crucial role, energy conservative schemes would be preferable to upwind methods. Mittal & Moin (1997) also pointed out an issue associated with the use of central difference methods is that simulations can be sensitive to numerical factors such as grid discontinuities and outflow boundary conditions. Consequently, grid generation and boundary conditions have to be designed with extreme care. The reader is referred to Kravchenko & Moin (1997) for further discussion of these and related issues.

Vreman *et al.* (1997) recently considered several subgrid models in LES of a temporal mixing layer. The convective terms in the filtered Navier–Stokes equations were discretized using a fourth-order method and the viscous terms were approximated using second-order central differences. Six SGS models were tested in the calculations, including the Smagorinsky model and various formulations of dynamic models. The dynamic models were found to yield more accurate results than the non-dynamic models because the dynamic procedure provides a mechanism to dissipate energy from resolved to subgrid scales. Vreman *et al.* (1997) concluded that, overall, the dynamic mixed model provided the best performance when compared with filtered DNS results.

These previous efforts, and similar studies performed by other researchers, have provided important guidelines for further application of LES as a tool to predict and investigate complex turbulent flows. As will be shown in §§ 2 and 3, the simulations presented in this paper have been carefully constructed and executed to establish the accuracy and validity of the computational approach.

The remainder of this paper is organized towards achieving the objectives described in § 1.1. A detailed description of the overall computational approach is first presented in § 2, with the governing equations and subgrid-scale models described in § 2.1. Time-dependent turbulent boundary conditions are required for simulation of the disk flow and this issue is addressed in § 2.2. In order to analyse the simulation results with confidence, it is necessary to establish the accuracy of the LES prior to an examination of the underlying physics. This task is addressed in § 3 where predictions of the mean velocity and second-order statistics for six parameter cases are thoroughly compared with the data of Littell & Eaton (1994). As shown in § 3, although some minor differences between LES predictions and measurements do exist, the simulations reproduce the mean and second-order statistics to very good accuracy and establish the validity of the computational approach for the subsequent discussion of single-point statistical properties in § 4.1 and analysis of structural measures in § 4.2.

2. Simulation overview

2.1. *Governing equations and subgrid model*

In LES, mass and momentum conservation is enforced for the large-scale resolved variables, which are obtained by filtering the Navier–Stokes equations. The filtered continuity and Navier–Stokes equations in a cylindrical system are,

$$\frac{\partial \overline{u}_z}{\partial z} + \frac{1}{r}\frac{\partial (r\overline{u}_r)}{\partial r} + \frac{1}{r}\frac{\partial \overline{u}_\theta}{\partial \theta} = 0, \tag{2.1}$$

$$\frac{\partial \overline{u}_r}{\partial t} = -\frac{\partial \overline{p}}{\partial r} + \frac{\partial}{\partial z}(\overline{s}_{13} - \overline{u}_r\overline{u}_z) + \frac{1}{r}\frac{\partial}{\partial r}(r\overline{s}_{11} - r\overline{u}_r\overline{u}_r) + \frac{1}{r}\frac{\partial}{\partial \theta}(\overline{s}_{12} - \overline{u}_r\overline{u}_\theta) - \left(\frac{\overline{s}_{22}}{r} - \frac{\overline{u}_\theta\overline{u}_\theta}{r}\right), \tag{2.2}$$

$$\frac{\partial \overline{u}_\theta}{\partial t} = -\frac{1}{r}\frac{\partial \overline{p}}{\partial \theta} + \frac{\partial}{\partial z}(\overline{s}_{23} - \overline{u}_\theta\overline{u}_z) + \frac{1}{r}\frac{\partial}{\partial r}(r\overline{s}_{12} - r\overline{u}_\theta\overline{u}_r) + \frac{1}{r}\frac{\partial}{\partial \theta}(\overline{s}_{22} - \overline{u}_\theta\overline{u}_\theta) + \left(\frac{\overline{s}_{12}}{r} - \frac{\overline{u}_\theta\overline{u}_r}{r}\right), \tag{2.3}$$

$$\frac{\partial \overline{u}_z}{\partial t} = -\frac{\partial \overline{p}}{\partial z} + \frac{\partial}{\partial z}(\overline{s}_{33} - \overline{u}_z\overline{u}_z) + \frac{1}{r}\frac{\partial}{\partial r}(r\overline{s}_{13} - r\overline{u}_z\overline{u}_r) + \frac{1}{r}\frac{\partial}{\partial \theta}(\overline{s}_{23} - \overline{u}_z\overline{u}_\theta). \tag{2.4}$$

In (2.1)–(2.4), an overbar denotes the variable filtered at the grid level. Lengths in (2.1)–(2.4) are normalized by the radius r_m (defined as $(r_1 + r_2)/2$, see figure 1*b*), velocities by the disk speed ωr_m. The Reynolds number is then $Re = \omega r_m^2/\nu$. The stresses in (2.2)–(2.4) are given by,

$$\left.\begin{aligned}
\overline{s}_{11} &= 2\left(\frac{1}{Re} + \nu_T\right)\frac{\partial \overline{u}_r}{\partial r} - \mathscr{L}^m_{11},\\
\overline{s}_{12} &= \left(\frac{1}{Re} + \nu_T\right)\left(\frac{\partial \overline{u}_\theta}{\partial r} + \frac{1}{r}\frac{\partial \overline{u}_r}{\partial \theta} - \frac{\overline{u}_\theta}{r}\right) - \mathscr{L}^m_{12},\\
\overline{s}_{22} &= 2\left(\frac{1}{Re} + \nu_T\right)\left(\frac{\overline{u}_r}{r} + \frac{1}{r}\frac{\partial \overline{u}_\theta}{\partial \theta}\right) - \mathscr{L}^m_{22},\\
\overline{s}_{23} &= \left(\frac{1}{Re} + \nu_T\right)\left(\frac{\partial \overline{u}_\theta}{\partial z} + \frac{1}{r}\frac{\partial \overline{u}_z}{\partial \theta}\right) - \mathscr{L}^m_{23},\\
\overline{s}_{33} &= 2\left(\frac{1}{Re} + \nu_T\right)\frac{\partial \overline{u}_z}{\partial z} - \mathscr{L}^m_{33},\\
\overline{s}_{13} &= \left(\frac{1}{Re} + \nu_T\right)\left(\frac{\partial \overline{u}_r}{\partial z} + \frac{\partial \overline{u}_z}{\partial r}\right) - \mathscr{L}^m_{13}.
\end{aligned}\right\} \tag{2.5}$$

Note that the subgrid-scale stress arising from the filtering operation can be decomposed in terms of the modified Leonard, cross, and SGS Reynolds stresses (Germano 1986). In (2.1), the modified Leonard term is $\mathscr{L}^m_{ij} = \overline{\overline{u}_i\overline{u}_j} - \overline{\overline{u}}_i\overline{\overline{u}}_j$ and an eddy viscosity hypothesis has been used to model the modified cross and Reynolds stresses where ν_T is the SGS eddy viscosity. Finally, it should also be noted that the filtered pressure $\overline{p}$ includes the trace of the subgrid stress.

In this study, three subgrid models are used: the dynamic eddy viscosity model of Germano *et al.* (1991), the dynamic mixed model of Zang, Street & Koseff (1993), and the dynamic mixed model of Vreman *et al.* (1994). These three closures can be uniformly expressed as,

$$\nu_T = C\overline{\Delta}^2|\overline{S}|, \quad C = -\frac{1}{2}\frac{\langle (L_{ij} - H_{ij})M_{ij}\rangle_\theta}{\langle M_{ij}M_{ij}\rangle_\theta}, \quad |\overline{S}| = \sqrt{2\overline{S}_{ij}\overline{S}_{ij}}, \tag{2.6}$$

where

$$M_{ij} = \widehat{\overline{\Delta}}^2|\widehat{\overline{S}}|\widehat{\overline{S}}_{ij} - \overline{\Delta}^2\widehat{|\overline{S}|\overline{S}_{ij}}, \qquad L_{ij} = \widehat{\overline{u}_i\overline{u}_j} - \widehat{\overline{u}}_i\widehat{\overline{u}}_j. \tag{2.7}$$

The SGS stress τ_{ij} is,

$$\tau_{ij} - \frac{\delta_{ij}}{3}\tau_{kk} = \mathscr{L}^m_{ij} - \frac{\delta_{ij}}{3}\mathscr{L}^m_{kk} - 2\nu_T\overline{S}_{ij}, \tag{2.8}$$

and the large-scale strain rate tensor, S_{ij}, is,

$$\left.\begin{aligned} \overline{S}_{11} &= \frac{\partial\overline{u}_r}{\partial r}, \quad \overline{S}_{12} = \frac{1}{2}\left(\frac{\partial\overline{u}_\theta}{\partial r} + \frac{1}{r}\frac{\partial\overline{u}_r}{\partial\theta} - \frac{\overline{u}_\theta}{r}\right), \\ \overline{S}_{22} &= \left(\frac{\overline{u}_r}{r} + \frac{1}{r}\frac{\partial\overline{u}_\theta}{\partial\theta}\right), \quad \overline{S}_{23} = \frac{1}{2}\left(\frac{\partial\overline{u}_\theta}{\partial z} + \frac{1}{r}\frac{\partial\overline{u}_z}{\partial\theta}\right), \\ \overline{S}_{33} &= \frac{\partial\overline{u}_z}{\partial z}, \quad \overline{S}_{13} = \frac{1}{2}\left(\frac{\partial\overline{u}_r}{\partial z} + \frac{\partial\overline{u}_z}{\partial r}\right). \end{aligned}\right\} \tag{2.9}$$

In the mixed model formulations of Zang *et al.* (1993) and Vreman *et al.* (1994), the tensor H_{ij} is evaluated as,

$$H_{ij} = \widehat{\overline{\overline{u}}_i\overline{\overline{u}}_j} - \widehat{\overline{\overline{u}}}_i\widehat{\overline{\overline{u}}}_j, \quad \text{or} \quad H_{ij} = \widehat{\overline{\overline{u}}_i\overline{\overline{u}}_j} - \widehat{\overline{\overline{u}}}_i\widehat{\overline{\overline{u}}}_j - (\widehat{\overline{u}_i\overline{u}_j} - \widehat{\overline{\overline{u}}}_i\widehat{\overline{\overline{u}}}_j), \tag{2.10}$$

respectively. Note that when the dynamic eddy viscosity model is used instead of the mixed models, $\mathscr{L}^m_{ij}$ is not explicitly computed, but rather presumed to be closed using the eddy viscosity part of the model.

In (2.7) and (2.10), $\widehat{\cdot}$ represents a filtering operation at the 'test filter' level (see Germano *et al.* 1991). In this work, the test-filter width, $\widehat{\overline{\Delta}}$, was twice the grid-filter width, $\overline{\Delta}$. Filtering was applied in the tangential and radial directions and the grid-filter width was assumed to be equal to the grid spacing in these directions. Multiple filtering operations, e.g. test-grid filter, $\widehat{\overline{\cdot}}$, and grid-grid filter, $\overline{\overline{\cdot}}$, were performed sequentially. A top-hat filter was used at the test-filter level; numerical integration as required for the filtering operations was performed using Simpson's rule. A clipping function was used to ensure non-negative values of C following the streamwise averaging applied to (2.6), where $\langle\cdot\rangle_\theta$ indicates an average taken in the tangential direction (see also Akselvoll & Moin 1996). The effects of clipping in two- and three-dimensional boundary-layer simulations were discussed in Wu & Squires (1998*a*, *b*). For further discussion of filtering, both in the dynamic procedure and LES, the reader is referred to Vreman *et al.* (1997) and Vasilyev, Lund & Moin (1998).

2.2. *Boundary conditions*

As discussed in § 1, the interest of the present investigation is in the fully turbulent disk flow at $Re = 6.5 \times 10^5$ ($Re_{\delta_2} = 2660$). At this Reynolds number, it would be difficult

to incorporate into the calculation the region of laminar-to-turbulent transition. For direct numerical simulations of flat-plate boundary-layer transition and discussion of the associated issues, see Rai & Moin (1993) and Ducros, Comte & Lesieur (1996). In this work, it is assumed that the residual effect of transition on turbulence statistics and structure is negligible. Support for this assumption can be found in the recent work of Lingwood (1996, 1997) on the stability characteristics of the disk flow boundary layer. Lingwood's work suggests that transition to turbulence occurs by an absolute instability, and thus the final state determined by nonlinear effects will be relatively independent of the transition process.

In order to solve the governing equations (2.1)–(2.4) in a computational domain, as shown in figure 1(*b*), time-dependent turbulent velocities must be specified at the two radial planes $r = r_1$ and $r = r_2$. These radial planes are not the same as the streamwise inflow/outflow positions typically encountered in other spatially developing flows. While periodic conditions are applicable along the (streamwise) tangential direction, they are inappropriate in the radial direction because of the entrainment from above the disk surface.

As pointed out by Littell & Eaton (1994), except near transition, there is a relatively slow variation of turbulence statistics along the radial direction. Using empirical correlations it is possible to estimate the growth of the boundary layer, and hence the rate of change in turbulence lengthscales, across the radial span of the computational domain. According to Schlichting (1979), the boundary-layer thickness in the disk 3DTBL is approximately,

$$\delta = 0.52 r Re^{-1/5} = 0.52 r^{3/5} (\nu/\omega). \tag{2.11}$$

Thus, for the present case in which the radial dimension $r_2 - r_1 = 2\delta_{r_1}$ (cf. figure 1*b*), the ratio of boundary-layer thicknesses at the two radial planes is,

$$\frac{\delta_{r_2}}{\delta_{r_1}} = \frac{(r_1 + 2\delta_{r_1})^{3/5}}{r_1^{3/5}} = [1 + 1.04 r_1^{-2/5} (\nu/\omega)^{1/5}]^{3/5} = (1 + 1.04 Re_{r_1}^{-1/5})^{3/5}. \tag{2.12}$$

For the Reynolds number considered in this study ($Re = 6.5 \times 10^5$), this ratio is $\delta_{r_2}/\delta_{r_1} \approx 1.04$, indicating that the growth in the radial direction is indeed small. Increasing the Reynolds number would further lower this ratio.

The weak dependence of boundary-layer lengthscales with the radial coordinate, in turn, suggests application of quasi-periodic boundary conditions similar to those developed by Spalart (1988) for two-dimensional boundary-layer simulations. To account for streamwise inhomogeneity, Spalart introduced a non-Cartesian coordinate system (new independent variables), and decomposed the turbulent signal into mean and fluctuating parts (new dependent variables). The fluctuating part is formed by a product of the r.m.s. velocity and a signal which is assumed to be periodic along the new coordinate line in the streamwise direction. Growth terms are added to the transformed Navier–Stokes equations. Streamwise derivatives of the mean and r.m.s. values appearing in the new governing equations are evaluated with the aid of the mean and r.m.s. results from an upstream station, which are in turn obtained through a separate simulation. Using this method, Spalart (1988) successfully performed direct numerical simulations of two-dimensional boundary layers at momentum thickness Reynolds numbers ranging from 225 to 1410.

Recently, the method of Spalart (1988) was modified by Lund, Wu & Squires (1998) for simulation of spatially developing boundary layers. The 'modified Spalart method' developed by Lund *et al.* (1998) generates its own inflow conditions through

a sequence of operations where the velocity field at a downstream station is rescaled and re-introduced at the inlet. No coordinate transformation is made and the original dependent variables (velocity and pressure), as well as the inflow–outflow structure are preserved. At the inflow station and another downstream location, the velocity components are decomposed as in Spalart (1988). The fluctuating part is formed by a product of the friction velocity and a signal which is assumed to be periodic along the streamwise direction. The mean velocities at the downstream and upstream stations are further assumed to be related with each other through inner–outer scaling laws similar to those discussed in Spalart (1988). The method of Lund *et al.* (1998) has been successfully used as an auxiliary simulation for generation of inflow conditions for subsequent predictions of complex spatially developing boundary layers (e.g. see Wang & Moin 1997; Wu & Squires 1998*a–c*).

The scheme used for generation of turbulent boundary conditions at coordinate planes $r = r_1$ and $r = r_2$ in the disk is based on a further modification of the method of Lund *et al.* (1998), taking into account the uniqueness of the disk flow. Similarly to Lund *et al.* (1998), no coordinate transformation is made and the original dependent variables are preserved. The specific steps are,

1. At the beginning of each timestep $t + \Delta t$, the instantaneous velocity fields are decomposed into a mean and fluctuating part,

$$\overline{u}_i(r,\theta,z,t) = \langle \overline{u}_i \rangle_\theta(r,z) + \langle \overline{u}_i'^2 \rangle_\theta^{1/2}(r,z)\overline{u}'_{i,P}(r,\theta,z,t) \quad (i = z,r,\theta), \tag{2.13}$$

where $\overline{u}'_{i,P}(r,\theta,z,t)$ is the time-dependent part of the signal that is assumed to be periodic at $r = r_1$ and $r = r_2$. Note that subscript i denotes the velocity component in the i direction, P refers to periodic, and (r,θ,z,t) indicates signal dependence. The mean and r.m.s. velocity profiles are $\langle \overline{u}_i \rangle_\theta(r,z)$ and $\langle \overline{u}_i'^2 \rangle_\theta^{1/2}(r,z)$, respectively, and are calculated during the simulation using an average in the θ-direction and running average in time.

2. The periodic signal $\overline{u}'_{i,P}(r,\theta,z,t)$ from the last timestep is then applied at the two radial boundary planes $r = r_1$ and $r = r_2$ at the new timestep in order to generate a time-dependent velocity field. The velocity profile at the two radial boundaries can then be expressed as,

$$\overline{u}_i(r_1,\theta,z,t+\Delta t) = \langle \overline{u}_i \rangle_\theta(r_1,z) + \langle \overline{u}_i'^2 \rangle_\theta^{1/2}(r_1,z)\overline{u}'_{i,P}(r \to r_2,\theta,z,t), \tag{2.14}$$

$$\overline{u}_i(r_2,\theta,z,t+\Delta t) = \langle \overline{u}_i \rangle_\theta(r_2,z) + \langle \overline{u}_i'^2 \rangle_\theta^{1/2}(r_2,z)\overline{u}'_{i,P}(r_1 \leftarrow r,\theta,z,t), \tag{2.15}$$

where $r_1 \leftarrow r$ and $r \to r_2$ represent radial stations adjacent to the two boundary planes r_1 and r_2, respectively. This is necessary since, unlike the treatment of strictly periodic conditions as in the homogeneous tangential direction, a simple interchange of the periodic signal $\overline{u}'_{i,P}$ between $r = r_1$ and $r = r_2$ would result in a limit cycle in the inhomogeneous radial direction. An analogous situation does not arise in the method of Lund *et al.* (1998) because only the downstream periodic signal is supplied at the inlet, and there is no need for a two-way exchange.

3. The time-independent mean and r.m.s. values appearing in (2.14)–(2.15) are calculated during the simulation through linear extrapolation of the corresponding mean and r.m.s. values at the interior radial plane $r = r_m$ (cf. figure 1*b*).

4. Entrainment along the top of the computational domain is obtained through a mass balance, i.e. the fluid being entrained from infinity towards the disk makes up

for the net increase in the flux along the radial direction (see figure 1),

$$\overline{u}_z(r,\theta,z\to\infty,t+\Delta t)=\frac{\iint \overline{u}_r(r_1,\theta,z,t+\Delta t)\,\mathrm{d}S_{r_1}-\iint \overline{u}_r(r_2,\theta,z,t+\Delta t)\,\mathrm{d}S_{r_2}}{\iint \mathrm{d}S_{z\to\infty}} \quad (2.16)$$

where $\iint \overline{u}_r(r_1,\theta,z,t+\Delta t)\,\mathrm{d}S_{r_1}$ is the mass flux through the coordinate plane $r=r_1$ and $\iint \mathrm{d}S_{z\to\infty}$ is the area of the upper surface of the computational domain. Note that it is assumed that $\overline{u}_z(z\to\infty)$ has negligible spatial variation over the upper surface of the annular domain.

The boundary treatment outlined above represents an approximation of the physical problem, but can be regarded as necessary at present to achieve a feasible computational problem. The wall-normal derivatives of the radial and tangential velocities along the upper surface of the computational domain are prescribed as zero. No-slip boundary conditions are applied at the disk surface $z=0$, and periodic conditions are applied along the (streamwise) tangential direction.

2.3. *Numerical method and computational details*

The governing equations (2.1)–(2.4) together with the boundary conditions outlined in § 2.2, were solved using a semi-implicit fractional step method in cylindrical coordinates. Second-order central differences were used for approximation of spatial derivatives on a staggered grid, together with a mixed explicit/implicit time advancement of the discretized equations. The continuity constraint was enforced by solving the Poisson equation for pressure using fast transforms along the homogeneous streamwise direction together with successive line over relaxation in the other two inhomogeneous directions. The numerical scheme is essentially the same as that used by Akselvoll & Moin (1996) in LES of a confined circular jet. In one simulation, streamwise derivatives were calculated using spectral discretization. For this hybrid spectral/finite-difference calculation, the streamwise velocity is collocated accordingly at the pressure node, and dealiasing is performed using the two-thirds rule.

Prior to prediction of the turbulent boundary layer, simulations were first performed in the laminar regime to validate the overall computational approach against the similarity solution. Calculations were performed at two Reynolds numbers, $Re=1.0\times10^3$ and 1.0×10^4; the size of the computational domain was $20\delta_l\times15\delta_l\times10\delta_l$ in the tangential (streamwise), wall-normal, and radial directions, respectively, where δ_l is the characteristic laminar lengthscale $(\nu/\omega)^{1/2}$ (see Schlichting 1979). In the laminar flow, the initial velocities u_r, u_z, and u_θ were zero. From the initial instant, the governing equations were integrated using a grid size of $5\times65\times33$ in the streamwise, wall-normal and radial directions, respectively. The governing equations, boundary conditions, and numerical scheme used in simulation of the laminar flow are the same as described in §§ 2.1 and 2.2, except that the fluctuating part in the radial boundary conditions vanishes.

In the laminar regime, the boundary layer has a constant thickness with no radial variation. The streamwise and radial velocity profiles will then collapse after proper scaling, while the wall-normal velocity should exhibit no dependence on the radial coordinate. Figure 3 compares the predicted velocity components in the laminar boundary layer with the numerical results in Schlichting (1979) obtained using von Kármán's similarity approach. The figure shows that the present numerical scheme reproduces the similarity solution and the profiles at the two Reynolds numbers are identical. Noteworthy is that the present mass-conservation based scheme reaches the

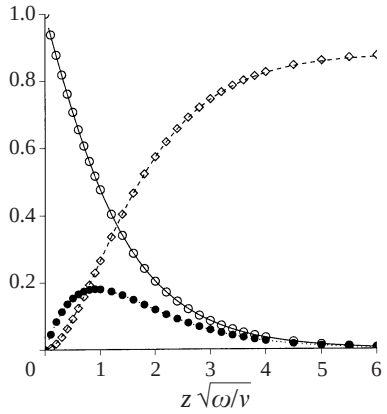

FIGURE 3. Velocity profiles in the three-dimensional laminar boundary layer over a rotating disk; symbols: similarity solution; lines: present simulations at $Re = 1.0 \times 10^3$ and 1.0×10^4. ○ ——, $u_\theta/\omega r$; ● ···, $u_r/\omega r$; ◇ - - -, $-u_z/(\nu\omega)^{1/2}$.

correct balance between radial mass flux and axial entrainment, as evident in the precise prediction of the laminar entrainment velocity. Starting from zero radial mass flux and zero entrainment at $t = 0$, the computation eventually yields the correct mass flux at planes $r = r_1$ and r_2 (cf. figure 1) so that their difference yields the same axial velocity $u_z(z)$ as obtained from the similarity solution.

LES calculations of the rotating disk 3DTBL were then performed at $Re = 6.5 \times 10^5$ corresponding to a momentum thickness Reynolds number $Re_{\delta_2} = 2660$. The height of the computational domain is $23\delta_2$ measured from the disk surface ($z = 0$), where δ_2 is the turbulent boundary-layer momentum thickness. The tangential and radial dimensions of the computational domain are $138\delta_2$ and $23\delta_2$, respectively. At $Re_{\delta_2} = 2660$, the ratio of the boundary-layer momentum thickness δ_2 to viscous lengthscale ν/u^* is 118. Thus, the tangential and radial dimensions of the computational domain are approximately 16 000 and 2700 wall units, respectively. As indicated by the two-point spatial correlations discussed in § 4.2, the tangential dimension is adequate to avoid contamination of the solution by periodic end conditions. The radial dimension is also sufficient since turbulence structures in this direction have lengthscales less than about 1000 wall units. It should also be noted that use of the approximate quasi-periodic boundary conditions presents difficulties when the radial dimension is further increased. For the turbulence simulation, the initial velocities $\overline{u}_r$ and $\overline{u}_z$ were prescribed as zero and the initial tangential component $\overline{u}_\theta$ was prescribed using the Reichardt correlation for zero pressure gradient boundary layers (Hinze 1975), superimposed with random fluctuations. Uniform grid spacings were applied in the tangential and radial directions, and hyperbolic stretching is used to cluster points near the wall. At $Re_{\delta_2} = 2660$ one viscous timescale ν/u^{*2} is equivalent to 0.2 inertial time units, $\delta_2/\omega r$. From the initial instant, the governing equations for the large-scale field were integrated to steady state at a timestep about one viscous timescale. Statistically steady state was reached after about 5200 inertial time units. Results were then sampled over a period of another 2600 inertial time units. Most of the results discussed in §§ 3 and 4 are presented in a rotating coordinate system. Velocities in the rotating coordinates are related to their counterparts in the laboratory system via $v_r = -u_r$, $v_\theta = \omega r - u_\theta$, and $v_z = u_z$ (cf. figure 1*b*).

Case	(r, θ, z)	Δr^+	$(r\Delta\theta)^+$	Δz^+_{min}	Model
1	(65,129,75)	41	126	1.0	Vreman
2	(65,259,75)	41	63	0.5	Vreman
3	(65,129,75)[#]	41	126	1.0	Germano
4	(65,129,75)	41	126	1.0	Germano
5	(65,129,75)	41	126	1.0	Zang
6	(65,129,75)	41	126	1.0	No model

TABLE 1. Summary of numerical parameters.

[#] Spectral discretization in the tangential direction.

3. Simulation validation

A series of calculations were performed to validate the overall computational approach and construct a foundation upon which further analysis can be performed with confidence. Details of the numerical parameters used in the validation tests are summarized in table 1.

As shown in the table, the first grid point along the wall-normal axis was within one wall unit for all simulations, with Case 2 having more points distributed in the region near the disk surface. Compared to Case 1, the streamwise resolution in Case 2 was refined by a factor of two. Case 3 uses the same resolution as Case 1 but with spectral discretization in the streamwise direction. Results from these cases will be used to demonstrate that the mean and second-order statistics resolved in the LES have converged to an acceptable level with respect to improved grid resolution, which would in turn suggest that the large-scale motions in the flow have been reasonably well resolved. An absolute invariance in LES with grid refinement may not be possible unless explicit filtering is used to eliminate the high wavenumber contributions from scales smaller than a fixed filter width (see Vasilyev *et al.* 1998 for further discussion). Although not shown here, simulations with grids coarser than that used in Case 1 were also performed and the results suggested that coarser resolutions than those summarized in table 1 do not fall into an accurate resolution range, capable of adequately resolving the important large-scale fluctuations, which is one prerequisite for a successful large-eddy simulation. In Cases 4 and 5, calculations were performed using the dynamic eddy viscosity model of Germano *et al.* (1991), and the dynamic mixed model of Zang *et al.* (1993), respectively. The grid resolutions in Cases 4 and 5 are the same as in Case 1 (using the dynamic mixed model of Vreman *et al.* 1994). A simulation was also performed (Case 6) in which no subgrid model was used. These results allow assessment of the overall effect of the SGS model on LES predictions.

Mean flow and second-order statistics predicted in Cases 1–3 are compared with the data of Littell & Eaton (1994) in figure 4. The dependent variables are normalized by the disk velocity ωr. The wall-normal coordinate is normalized by the momentum thickness δ_2 based on $0.99\omega r$. Mean flow and turbulence statistics were obtained through averaging over time as well as along the homogeneous streamwise (tangential) direction. Since the momentum thickness Reynolds number Re_{δ_2} varies only 4% along the radial direction from 2610 to 2710, the statistics have a much weaker dependence on the radial coordinate after being normalized by the local disk velocity or local friction velocity (Littell & Eaton 1994). Thus, the results shown in figure 4 and in subsequent figures are the averaged profiles for $2610 < Re_{\delta_2} < 2710$.

Figure 4(*a*) shows the mean tangential and radial velocities. Throughout the bound-

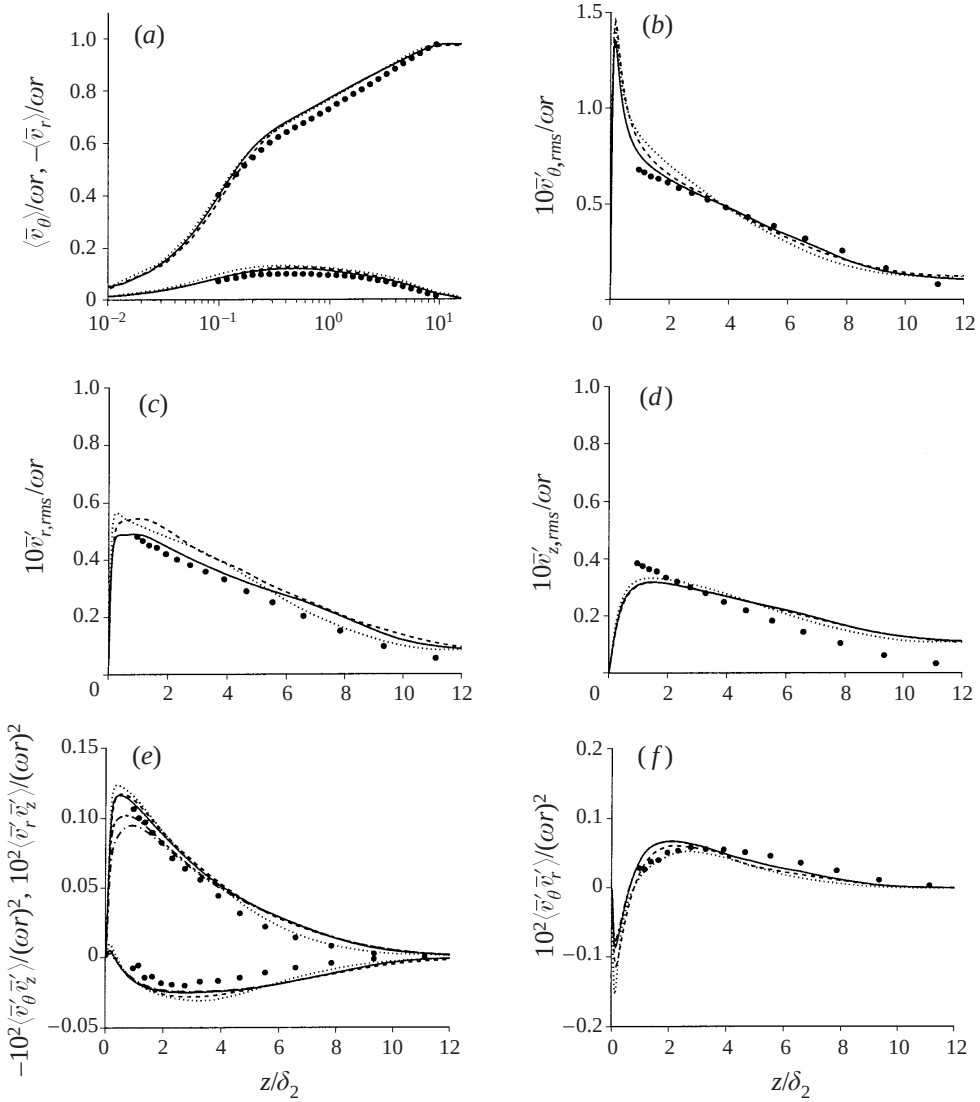

FIGURE 4. Comparison of LES predictions with experimental measurements. LES: ···, Case 1; ——, Case 2; - - -, Case 3; –·–, resolved shear stresses only in Case 2; – – –, resolved shear stresses and modelled subgrid contribution, but without the modified Leonard stresses in Case 2; •, Littell & Eaton (1994).

ary layer the predicted mean profiles from Cases 1, 2, and 3 nearly collapse and are in good agreement with the measurements of Littell & Eaton (1994). The largest discrepancy in the mean tangential velocity occurs in the logarithmic region with a maximum error less than 4% of the disk velocity. Based on the results of Case 2, one momentum thickness δ_2 is equivalent to 118 wall units. The predicted mean radial velocity has a peak value of $0.12\omega r$ located at $z^+ = 50$, compared to the peak location $z^+ = 47$ in the experiments of Littell & Eaton. The maximum error in the mean radial velocity occurs near the location of the peak crossflow with a magnitude less than $0.02\omega r$. Other important mean flow properties are summarized in table 2, where H is the boundary-layer shape factor. The friction velocity u^* from Littell & Eaton (1994)

	Case 1	Case 2	Case 3	Case 4	Case 5	Case 6	Littell & Eaton
$u^*/\omega r$	0.041	0.041	0.040	0.040	0.043	0.044	0.044
α	17°	16°	16°	17°	15°	14°	n/a
H	1.23	1.23	1.23	1.25	1.24	1.22	1.29

TABLE 2. Boundary-layer parameters.

was derived from a Clauser plot, the LES predictions were evaluated directly from the computed near-wall profiles. As seen in the table, on average, the skewing angle, α, that the wall shear stress vector makes with respect to the freestream is about 16° at $Re_{\delta_2} = 2660$, compared to a skewing of 39.6° in the laminar flow (Schlichting 1979).

Predictions of the resolved streamwise turbulence intensity from Cases 1–3 are compared with measurements in figure 4(*b*). As shown in the figure, $\overline{v}'_{\theta,rms}$ is sensitive to streamwise resolution in a region close to the disk surface, i.e. $0.5 < z/\delta_2 < 3$. Case 1 overpredicts the streamwise turbulence intensity in this region. The overprediction is reduced with a refinement in the streamwise grid spacing, and there is very good agreement with Littell & Eaton (1994) for the Case 2 prediction. Predictions of the radial and wall-normal fluctuating velocities are presented in figures 4(*c*) and 4(*d*), respectively. The agreement between LES predictions of $\overline{v}'_{r,rms}$ in figure 4(*c*) with measurements is good, with some small differences among the cases. The predicted wall-normal intensity is in fair agreement with Littell & Eaton (1994), and is relatively insensitive to changes in streamwise resolution. The underprediction of $\overline{v}'_{z,rms}$ in the near-wall region is common to LES calculations of wall-bounded flows and related to the anisotropy of the computational grid and subgrid-scale motions (e.g. see Scotti, Meneveau & Lilly 1993); the overprediction in the outer part of the boundary layer seems to be unique to the present calculations. Near the edge of the boundary layer, LES predictions of the turbulence intensities tend to be more isotropic than those measured by Littell & Eaton (1994).

Predictions of the primary turbulent shear stress $-\langle \overline{v}'_\theta \overline{v}'_z \rangle$ and the secondary shear stress $\langle \overline{v}'_r \overline{v}'_z \rangle$ are shown in figure 4(*e*). These two stresses appear in the Reynolds-averaged boundary-layer equations, and the vector formed by $-\langle \overline{v}'_\theta \overline{v}'_z \rangle$ and $\langle \overline{v}'_r \overline{v}'_z \rangle$ is parallel to the disk surface. Note the predicted turbulent shear stresses include the resolved large-scale fluctuations and the subgrid-scale contributions τ_{ij}. As defined in (2.8), τ_{ij} is composed of the part modelled by $-2\nu_T \overline{S}_{ij}$ and the modified Leonard term $\mathscr{L}^m_{ij}$. Figure 4(*e*) shows there is very good agreement between the predicted and measured turbulent shear stresses. The secondary shear stress $\langle \overline{v}'_r \overline{v}'_z \rangle$, although negative through most of the boundary layer, changes sign very close to the disk surface and reaches a minor positive peak. This is consistent with the conjecture made by Littell & Eaton (1994) that $\langle \overline{v}'_r \overline{v}'_z \rangle$ must change sign close to the wall in order to approach the radial wall shear stress. Figure 4(*e*) also shows profiles of the resolved component as well as the sum of resolved and modelled SGS stresses obtained from the Case 2 simulation. For the primary shear stress, the peak of the resolved-only profile is 20% lower than the peak in the profile which includes contributions from all the three sources, i.e. the resolved, modelled, and modified Leonard term contributions. For the secondary shear stress $\langle \overline{v}'_r \overline{v}'_z \rangle$, the differences among the three profiles are negligible. The other secondary shear stress $\langle \overline{v}'_\theta \overline{v}'_r \rangle$ is shown in figure 4(*f*). This component does not appear in the boundary-layer equation and is usually neglected in 3DTBL

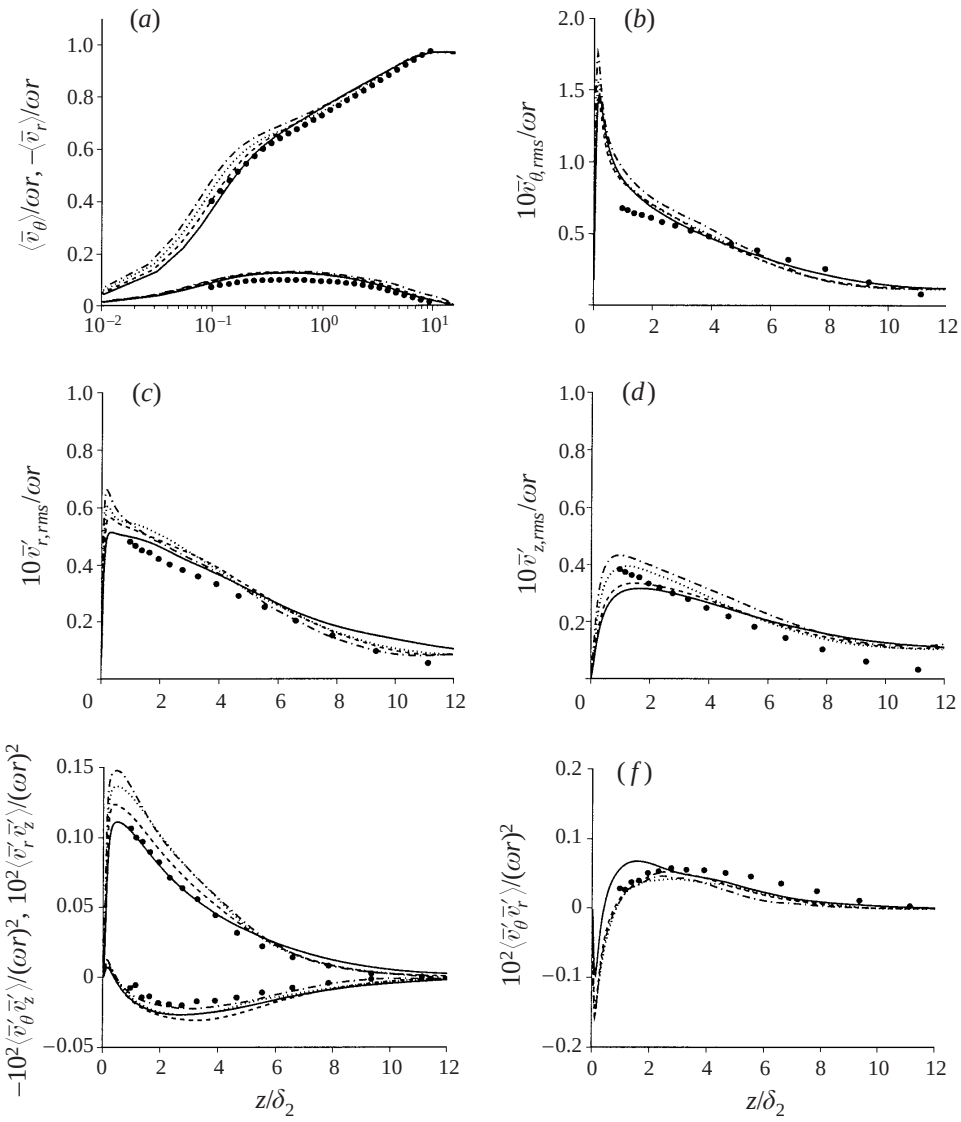

FIGURE 5. Comparison of LES predictions with experimental measurements. LES: ——, Case 4; · · ·, Case 5; - - -, Case 1; – · –, Case 6; •, Littell & Eaton (1994).

analysis (e.g. see Spalart 1989; Littell & Eaton 1994; Johnston & Flack 1996). Figure 4(*f*) shows the agreement between the LES predictions of $\langle\bar{v}'_\theta\bar{v}'_r\rangle$ and measurements is reasonable. Additional discussion of this particular shear stress is provided in § 4.1.

The overall effect of the SGS model on the mean flow and second-order statistics is shown in figure 5. Four sets of results from simulations using the same resolution are presented, which include calculations using the dynamic eddy viscosity model (Case 4), the dynamic mixed model of Zang *et al.* (1993) (Case 5), the dynamic mixed model of Vreman *et al.* (1994) (Case 1), and no-model results (Case 6). Figure 5(*a*) shows that near the wall, the no-model calculation overpredicts the mean streamwise velocity. Case 5 using the mixed model of Zang *et al.* (1993) yields similar overpredictions to the Case 6 results obtained without a subgrid model. Cases 1 and 4 predictions of

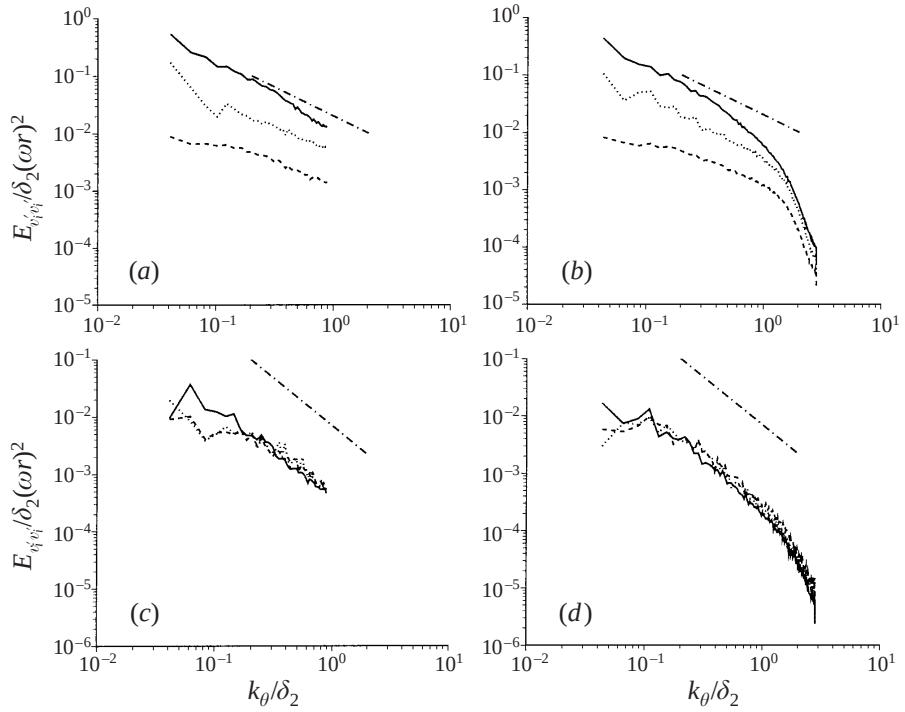

FIGURE 6. Streamwise energy spectrum. $\cdots$, radial; ——, tangential; - - -, wall-normal. $-\cdot-$, -1 slope in (*a*) and (*b*), $-5/3$ slope in (*c*) and (*d*). (*a*) Case 3, $z/\delta_2 = 0.5$; (*b*) Case 2, $z/\delta_2 = 0.5$; (*c*) Case 3, $z/\delta_2 = 8$; (*d*) Case 2, $z/\delta_2 = 8$.

the mean streamwise velocity are in better agreement with the data throughout the boundary layer. This is similar to the findings obtained by Vreman *et al.* (1994) in which a reduced level of SGS dissipation was obtained using the dynamic formulation of Zang *et al.* (1993), resulting in predictions similar to those from simulations using no subgrid model. Also apparent from figure 5(*a*) is that the predicted mean radial velocity is insensitive to the change of SGS models.

The predicted turbulence intensities are shown in figures 5(*b*)–5(*e*). The Case 6 prediction obtained without a subgrid model and the Case 5 results using the dynamic model of Zang *et al.* (1993) yield slightly higher near-wall fluctuation levels than the other two cases, analogous to the behaviour observed in the mean flow predictions (cf. figure 5*a*). The figure also shows that the differences among the cases are smaller for the tangential and radial fluctuations than for the wall-normal fluctuations. The predicted primary shear stress in figure 5(*e*) exhibits similar trends to the intensities, i.e. overprediction of the peak values for Case 5 and Case 6, and good agreement with measurements for the other two cases. Similarly to figure 4(*e*), the shear stress profiles include contributions from the modified Leonard term and eddy viscosity part of the model. Figures 5(*e*) and 5(*f*) also suggest that variations of the two secondary shear stress components with the change of SGS model are more complex than those of the mean flow, turbulence intensities, and the primary shear stress. Nevertheless, the overall agreement of the predicted secondary shear stresses with the experimental measurements of Littell & Eaton (1994) is still reasonably good.

Streamwise energy spectra are presented in figure 6 for wall-normal locations $z/\delta_2 = 0.5$ ($z^+ = 55$) and $z/\delta_2 = 8$ ($z^+ = 880$). Two sets of results are shown, i.e.

Case 3 predictions using the hybrid spectral/finite-difference scheme similar to that of Mittal & Moin (1997), and the finite-difference Case 2 calculations. Figures 6(*a*) and 6(*b*) show $E_{v_i'v_i'}$ acquired at $z/\delta_2 = 0.5$ for Cases 3 and 2, respectively. As summarized in Hinze (1975), it is possible to distinguish the spectral behaviour associated with two different types of motions. In the first instance, the vorticity of the main motion is small compared with the vorticity of the turbulence in the wavenumber range under consideration. Direct interaction between the main and turbulent motions becomes weak and finally zero. In an inertial subrange this implies Kolmogorov's $-5/3$ law. In the second instance, the vorticity of the main motion is comparable to the vorticity of the turbulence in the wavenumber range under consideration. Since the vorticity of the mean motion is large, the effect of its interaction with the turbulent motion predominates with respect to the viscous dissipation and eddy transfer. Energy spectra for the wavenumber range in which such an interaction occurs varies as k^{-1}. Although the development in Hinze (1975) applies to homogeneous turbulent shear flow, previous experiments have found similar spectral slopes in 2DTBLs (e.g. Perry, Henbest & Chong 1986). It is interesting that the disk boundary-layer spectra in figures 6(*a*) and 6(*b*) exhibit ranges which vary approximately as k_θ^{-1}. This is more apparent for the radial and wall-normal velocity fluctuations, and also for the azimuthal component prior to its drop off. Figures 6(*c*) and 6(*d*) show $E_{v_i'v_i'}$ acquired at $z/\delta_2 = 8.0$ for Cases 3 and 2, respectively. The spectra exhibit a reasonable $-5/3$ range.

Overall, there is good agreement between LES predictions of the mean flow and second-order statistics from Cases 1–4 and the measurements of Littell & Eaton (1994). The streamwise and radial mean and fluctuating velocities are in good agreement with measurements, with the largest discrepancy occurring in prediction of the wall-normal fluctuations. The primary and two secondary turbulent shear stresses are also in good agreement with Littell & Eaton (1994). One-dimensional energy spectra decay with approximately a -1 slope in the near-wall region and $-5/3$ range in the outer part of the boundary layer. The results in figures 4 and 5 have shown that the important large-scale fluctuations in the disk boundary layer have been reasonably resolved, as suggested by the weak dependence on grid refinement and change in subgrid model. Thus, while some small discrepancies do exist between calculation and experiment, predictions presented in this section demonstrate that the first objective discussed in § 1.1 has been achieved, i.e. accurate simulation of the 3DTBL over a rotating disk at $Re_{\delta_2} = 2660$ and evaluation of LES predictions using the data of Littell & Eaton (1994). The results will be used next to explore single-point statistics in § 4.1 and then analyse structural features of the flow in § 4.2.

4. Flow analysis

4.1. *Single-point statistical measures*

The derivative of the mean streamwise velocity from Case 2 is shown in figure 7, together with the measurements of Littell & Eaton (1994). Spalart (1989) pointed out that a rigorous definition of a logarithmic layer is a region within which $z^+ \mathrm{d}\langle\overline{v}_\theta\rangle^+/\mathrm{d}z^+$ takes the constant value $1/\kappa$. In a canonical two-dimensional boundary layer this region is bounded at both ends by values larger than $1/\kappa$, i.e. by the buffer and wake regions. Figure 7 shows that in the disk flow both LES predictions and measurements display a substantial logarithmic region as evident from $z^+ \mathrm{d}\langle\overline{v}_\theta\rangle^+/\mathrm{d}z^+$ taking nearly constant values very close to $1/\kappa$ within $50 < z^+ < 800$. It is also interesting to note

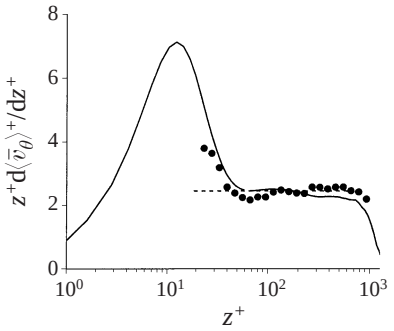

FIGURE 7. Derivative of the mean streamwise velocity. •, Littell & Eaton (1994); ---, $z^+\mathrm{d}\langle\bar{v}_\theta\rangle^+/\mathrm{d}z^+ = 1/0.41$; ——, Case 2.

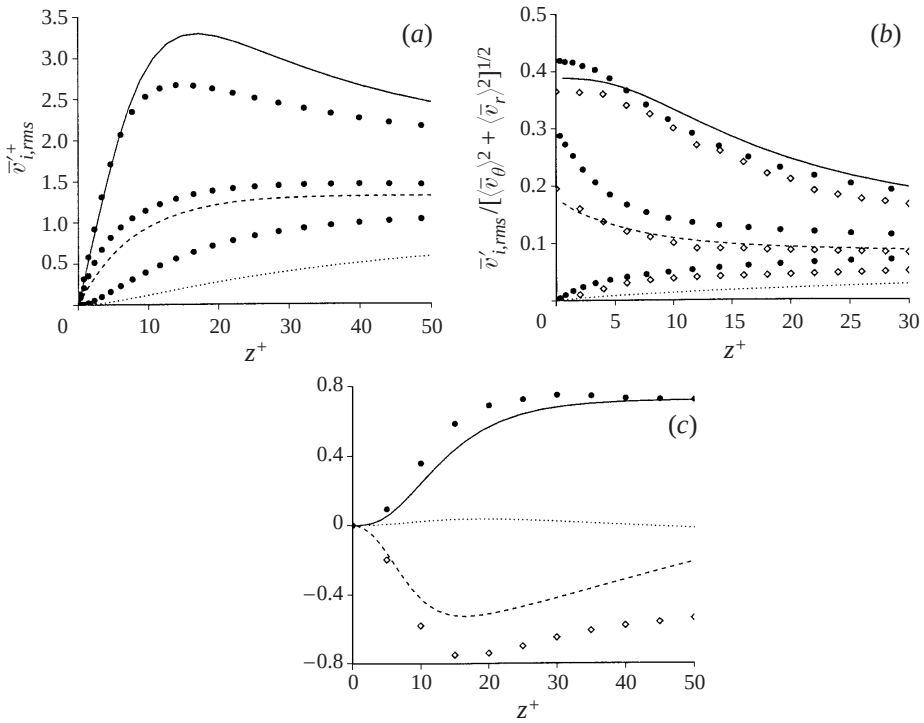

FIGURE 8. Near-wall behaviour of turbulence intensities (in *a* and *b*) and turbulent shear stresses (in *c*), lines: Case 2. In (*a*) and (*b*): •, DNS of two-dimensional boundary layer (Spalart 1988); ◇, DNS of channel flow (Kim *et al.* 1987); ——, streamwise; ···, wall-normal; ---, radial. In (*c*): •, $\{\langle\bar{v}'_\theta\bar{v}'_z\rangle^{+2} + \langle\bar{v}'_r\bar{v}'_z\rangle^{+2}\}^{1/2}$; ——, $-\langle\bar{v}'_\theta\bar{v}'_z\rangle^+$; ···, $\langle\bar{v}'_r\bar{v}'_z\rangle^+$; --- ◇, $\langle\bar{v}'_\theta\bar{v}'_r\rangle^+$. Symbols in (*c*) are DNS of three-dimensional boundary layer (Spalart 1989).

from the figure that, compared to two-dimensional turbulent boundary layers, the disk 3DTBL lacks a well-defined wake region since the high end of the constant $z^+\mathrm{d}\langle\bar{v}_\theta\rangle^+/\mathrm{d}z^+$ region is bounded by values smaller than $1/\kappa$, rather than larger values. A similar behaviour is also observed in other equilibrium 3DTBLs created over infinite geometries (Spalart 1989; Wu & Squires 1997).

Near-wall characteristics of the turbulence intensities and turbulent shear stresses in the disk flow are presented in figure 8, together with the DNS results of Spalart (1988,

1989) from zero-pressure gradient and three-dimensional boundary layers and Kim, Moin & Moser (1987) from turbulent channel flow. Figure 8(*a*) shows the intensities of the three velocity fluctuations relative to the friction velocity u^*. Similarly to Spalart (1988), the streamwise component peaks at about $z^+ = 15$ but with a larger maximum value of 3.3. The higher peak of $\overline{v}^{'+}_{rms,\theta}$ compared to the boundary-layer DNS is due both to errors in the computed friction velocity and numerical resolution. The radial component also resembles that of Spalart (1988) with a plateau about 1.3 in the region of $30 < z^+ < 50$. Figure 8(*b*) shows the turbulence intensities normalized by the magnitude of the local mean velocity, i.e. $\overline{v}^{'}_{i,rms}/[\langle\overline{v}_\theta\rangle^2 + \langle\overline{v}_r\rangle^2]^{1/2}$. As pointed out by Kim *et al.* (1987), the limiting values of these quantities should approach the wall values of the corresponding vorticity fluctuations normalized by the mean velocity gradient. The figure shows that the streamwise components in all three types of flow reach constant values (about 0.4) at the wall. The radial component $\overline{v}^{'}_{r,rms}/\langle\overline{v}_r\rangle$ has a limiting value 0.2, nearly identical to Kim *et al.* (1987), but smaller than Spalart (1988). Overall, the results shown in figure 8 suggest that the turbulence intensities in the near-wall region of a disk flow are not markedly different from their counterparts in other canonical two-dimensional flows.

Figure 8(*c*) shows the three shear stress components relative to u^{*2}. Also shown are the DNS results of Spalart (1989) obtained from a 3DTBL created by a rotating free-stream velocity vector. For the flow considered by Spalart (1989), only $\langle\overline{v}^{'}_\theta\overline{v}^{'}_r\rangle^+$ and the magnitude of the shear stress vector $\{\langle\overline{v}^{'}_\theta\overline{v}^{'}_z\rangle^{+2} + \langle\overline{v}^{'}_r\overline{v}^{'}_z\rangle^{+2}\}^{1/2}$ are shown since the stresses $\langle\overline{v}^{'}_\theta\overline{v}^{'}_z\rangle$ and $\langle\overline{v}^{'}_r\overline{v}^{'}_z\rangle$ are defined in a coordinate system not aligned with the freestream velocity (see Wu & Squires 1997 for further discussion). For the disk flow, the profile of $\{\langle\overline{v}^{'}_\theta\overline{v}^{'}_z\rangle^{+2} + \langle\overline{v}^{'}_r\overline{v}^{'}_z\rangle^{+2}\}^{1/2}$ collapses with that of the primary shear stress $-\langle\overline{v}^{'}_\theta\overline{v}^{'}_z\rangle^+$ because the other component $\langle\overline{v}^{'}_r\overline{v}^{'}_z\rangle^+$ is very small in the near-wall region. The figure shows that the magnitude of the shear stress vector parallel to the wall for the disk 3DTBL is similar to that of Spalart (1989) with a plateau around 0.7, smaller than the corresponding value in a two-dimensional boundary layer (e.g. 0.92 in the DNS of Spalart 1988). As in Spalart (1989), the secondary shear stress $\langle\overline{v}^{'}_\theta\overline{v}^{'}_r\rangle$ takes rather large values near the wall which is comparable or even larger than the magnitude of the shear stress vector parallel to the wall. The peak of $\langle\overline{v}^{'}_\theta\overline{v}^{'}_r\rangle^+$ is located at $z^+ = 15$ for both 3DTBLs. Spalart (1989) also pointed out that this particular component has a significant dependence on Reynolds number but has only a negligible effect on the mean momentum equation. Although not shown here, the ratio of the shear stress vector magnitude in planes parallel to the wall to twice the turbulence kinetic energy was nearly constant for $100 < z^+ < 800$ with a value about 0.14. In addition, the angle between the turbulent shear stress vector and strain rate vector in planes parallel to the disk surface was small, with a maximum difference of about 10° near the wall. Similar behaviour has been reported in other equilibrium 3DTBLs, such as the Ekman layer considered by Coleman *et al.* (1990) and the rotating 3DTBL of Spalart (1989).

4.2. *Structural measures*

4.2.1. *Disk flow structure*

The structural model of Littell & Eaton (1994) is based on the hypothesis that the overall shear-stress producing structure in the disk flow can be modelled as an appropriate alteration of that in a canonical two-dimensional boundary layer. Based on their measurements, Littell & Eaton (1994) proposed that the modification by the crossflow alters the relative strengths of ejections and sweeps arising from structures with different signs of streamwise vorticity. Specifically, their model considers a

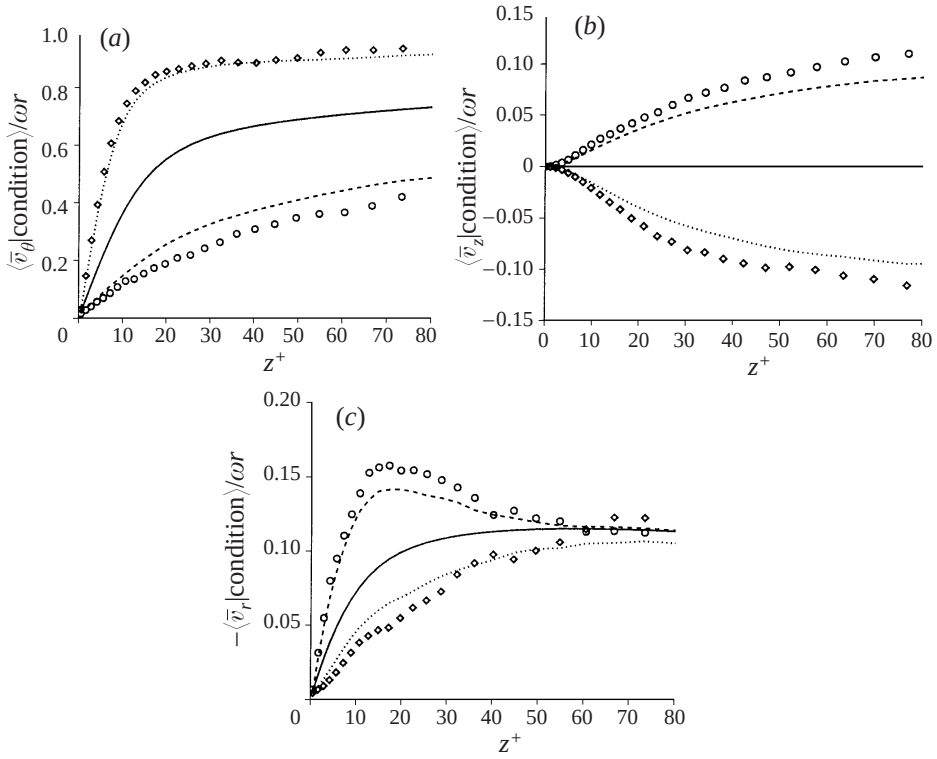

FIGURE 9. Conditionally averaged velocities. --- ○, averaged using the strong ejection condition $-\overline{v}'_\theta\overline{v}'_z > \beta\overline{v}'_{\theta,rms}\overline{v}'_{z,rms}$ and $\overline{v}'_z > 0$; $\cdots\diamond$, averaged using the strong sweep condition $-\overline{v}'_\theta\overline{v}'_z > \beta\overline{v}'_{\theta,rms}\overline{v}'_{z,rms}$ and $\overline{v}'_z < 0$; lines: $\beta = 6$; symbols: $\beta = 10$; ——, mean; (*a*) streamwise; (*b*) wall-normal; (*c*) radial.

subdivision of vortical structures into two classes (+ or −) according to the sign of streamwise vortices relative to that of the mean streamwise vorticity (see figure 2). Class + structures are those whose streamwise vortices have the same sign as the mean streamwise vorticity beneath the peak crossflow location. Class − structures refer to those whose streamwise vortices have opposite sign as the mean streamwise vorticity beneath the peak crossflow.

The model is then that Class + vortices are mostly responsible for strong sweep events, while Class − structures promote strong ejections. A consequence of this model is that beneath the location of the peak crossflow, conditionally sampled radial velocities should be smaller than the mean for strong sweep events, and the profile for strong ejections should be larger than the mean (cf. figure 2*b*). In support of this model, Littell & Eaton (1994) used the asymmetry of their conditionally sampled wall-normal fluctuating velocity upstream and downstream (in the radial direction) of shear-stress producing events. A direct examination of the model can be undertaken by measuring the conditionally averaged radial crossflow velocity for shear-stress producing events.

Figure 9 shows conditionally-averaged velocities occurring under strong ejection and sweep events. The criteria used in figure 9 to define strong ejections is $-\overline{v}'_\theta\overline{v}'_z > \beta\overline{v}'_{\theta,rms}\overline{v}'_{z,rms}$ and $\overline{v}'_z > 0$, while the criteria for strong sweeps is $-\overline{v}'_\theta\overline{v}'_z > \beta\overline{v}'_{\theta,rms}\overline{v}'_{z,rms}$ and $\overline{v}'_z < 0$. To check the consistency of the results, two values of β are used, i.e. $\beta = 6$ and 10. Note that since the ratio of shear stress $-\langle\overline{v}'_\theta\overline{v}'_z\rangle$ to the product of the intensities

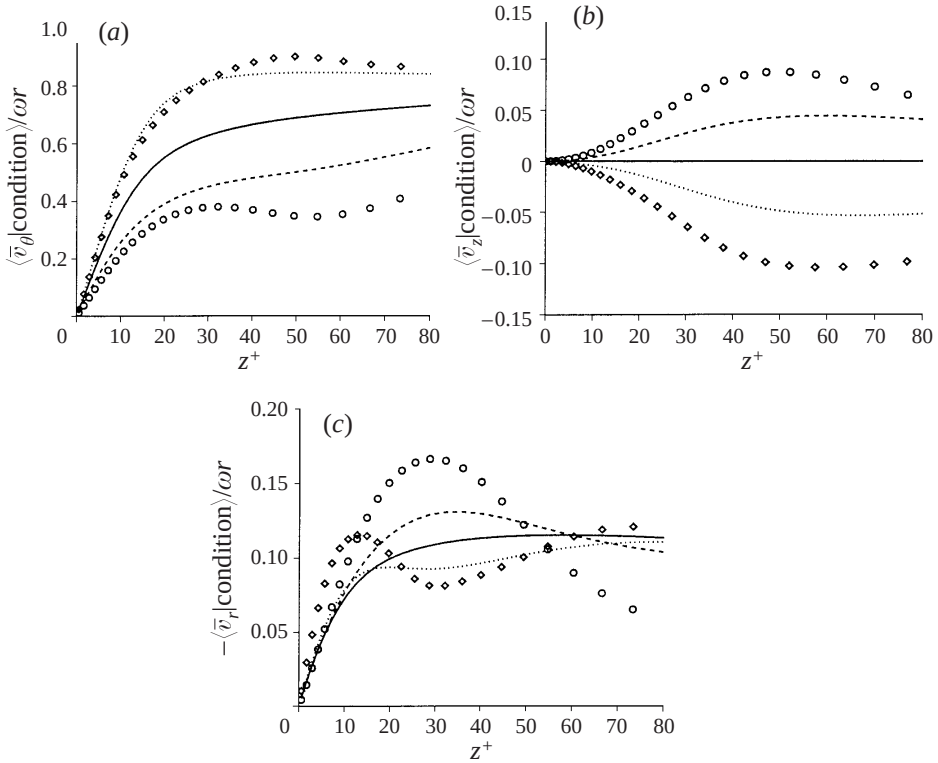

FIGURE 10. Conditionally averaged velocities. - - - ○, averaged using the strong ejection condition at the peak location of crossflow $z^+ = 50$: $-\bar{v}'_\theta \bar{v}'_z > \beta \bar{v}'_{\theta,rms} \bar{v}'_{z,rms}$ and $\bar{v}'_z > 0$; $\cdots \diamond$, averaged using the strong sweep condition at the peak location of crossflow $z^+ = 50$: $-\bar{v}'_\theta \bar{v}'_z > \beta \bar{v}'_{\theta,rms} \bar{v}'_{z,rms}$ and $\bar{v}'_z < 0$; lines: $\beta = 2$; symbols: $\beta = 10$; ——, mean; (*a*) streamwise; (*b*) wall-normal; (*c*) radial.

$\bar{v}'_{\theta,rms} \bar{v}'_{z,rms}$ is around 0.5 in the buffer region, these thresholds translate into requiring that the instantaneous shear stress be 12 and 20 times the mean primary shear stress, respectively. The profiles of the streamwise and wall-normal velocities in figures 9(*a*) and 9(*b*) show substantial differences between the mean and conditionally averaged profiles. This is consistent with the consensus discussed in Robinson (1991) that in most cases the variance of the measurable attributes of shear-producing structures about their mean values is very large (see also Kim & Moin 1986). Figure 9(*c*) shows that beneath the location of the peak crossflow, $z^+ = 50$, the conditionally averaged radial profile is larger than the unconditioned mean for strong ejection events, and has a deficit compared to the global profile for strong sweeps. There is also an indication that these two profiles intersect slightly above the location of the peak crossflow velocity, which is consistent with the structural model of Littell & Eaton (1994) as well as other conceptual models which coincide with canonical two-dimensional boundary-layer structure.

Figure 10 shows the conditionally averaged profiles for strong ejection and sweep events using a different set of criteria to those in figure 9. The criteria used in figure 10 to define strong ejections are $-\bar{v}'_\theta \bar{v}'_z > \beta \bar{v}'_{\theta,rms} \bar{v}'_{z,rms}$ and $\bar{v}'_z > 0$ at $z^+ = 50$, while the criteria for strong sweep events is $-\bar{v}'_\theta \bar{v}'_z > \beta \bar{v}'_{\theta,rms} \bar{v}'_{z,rms}$ and $\bar{v}'_z < 0$ at $z^+ = 50$, i.e. averaging is performed across the boundary layer whenever an ejection/sweep event is detected at the peak crossflow location. To again check the consistency of the results, two values of β are used, i.e. $\beta = 2$ and 10. Again, as shown in figure 10(*c*),

a large excess and a measurable deficit appear in the conditionally averaged radial velocity in the region $20^+ < z^+ < 50$ corresponding to the strong ejection and strong sweep events, respectively. Moreover, there is an intersection above $z^+ = 50$. This arises because, according to the model of Littell & Eaton (1994) illustrated in figure 2(*b*), above the peak crossflow location, Class − structures should reduce the radial velocity for strong ejections, and Class + structures should augment it for strong sweeps. The trend is a reverse of that beneath the peak crossflow.

4.2.2. *Structural similarities between 2DTBLs and 3DTBLs*

Although figures 9 and 10 have provided new proof in support of the 3DTBL structural model advanced by Littell & Eaton (1994), these results have not yet touched upon the important hypothesis made in their work, i.e. the arch-like vortex structure discussed in Robinson (1991) comprising the underlying structure of canonical two-dimensional boundary layers can be used as a baseline in the disk 3DTBL. As pointed out by Johnston & Flack (1996), this assumption has been accepted to date more or less as a fact based partly on intuition, partly on single-point statistics, and partly on visualizations which showed that low- and high-speed streaks in two-dimensional boundary layers are also present in many 3DTBLs. A similar example from the disk flow is presented in figure 11. Figure 11(*a*) shows isosurfaces of the instantaneous pressure fluctuation. Only regions corresponding to strong negative fluctuations are shown, corresponding to the low-pressure cores discussed in Robinson (1991). The figure shows at this particular instant that there exists a well-defined arch-like vortex structure in remarkable resemblance to that drawn in figure 2(*a*) for 2DTBLs (because of the quasi-periodic boundary condition applied in the radial direction, part of the longer leg near the r_2 boundary is displaced to the region near r_1). Isosurfaces of $Q = W_{ij}W_{ij} - S_{ij}S_{ij}$, where W_{ij} is the skew symmetric rate of rotation tensor, were also used to identify vortical structures. Using Q, however, did not yield a definitive visualization of structural features (see also Chong *et al.* 1996). On the other hand, identification of vortical motions such as the elongated structures described above by correspondence with regions of low pressure was more revealing. The reader is referred to Jeong *et al.* (1997) and references therein for further discussion of structural identification in turbulent boundary layers. Figure 11(*b*) shows contours of the instantaneous azimuthal velocity fluctuation $\overline{v}'_\theta/\omega r$ at $z^+ \approx 5$. Apparent in the figure are elongated regions of low- and high-speed fluid, associated with the streaklike character of the near-wall region of turbulent boundary layers. The streaks are not aligned with the azimuthal direction, rather, they are skewed away from the disk centre. Dimensions of the streak structures can be inferred by noting that the radial and azimuthal dimensions of the computational domain are 2700 and 16 000 wall units, respectively.

A quantitative illustration based on single-point measures of the similarity in the disk boundary layer and statistically two-dimensional flows is shown in figure 12. Shown in the figure is the contribution to the primary turbulent shear stress from each quadrant as a function of wall-normal distance, following the quadrant analysis of Kim *et al.* (1987). As shown in the figure, the overall similarity between the LES predictions and DNS results of Kim *et al.* (1987) is striking, taking into account of the significant difference in the Reynolds number. Both flows display the dominance of the ejection event (second quadrant) away from the wall with sweep events (fourth quadrant) dominating in the wall region. The limiting wall values in the disk flow for ejections and sweeps are 0.9 and 0.5, respectively, compared to 1.1 and 0.5 in the channel flow. Near the boundary-layer edge the ejection profile (second quadrant)

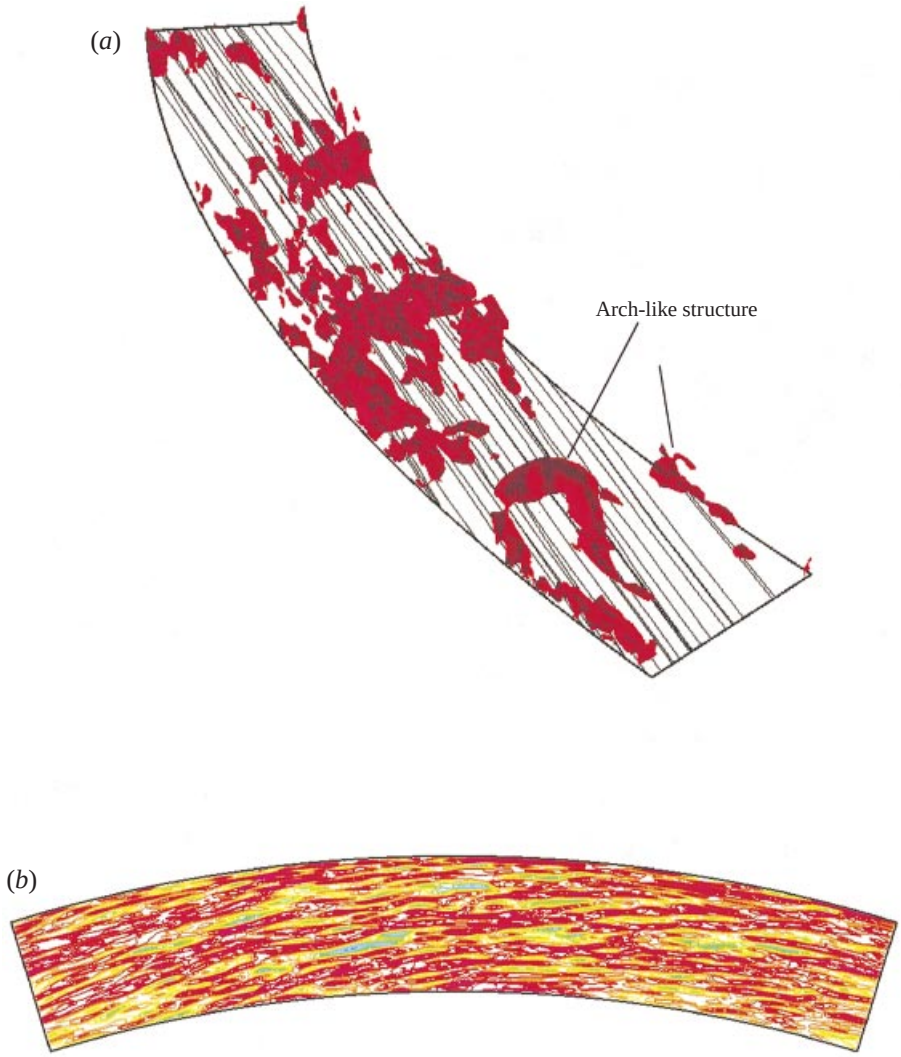

FIGURE 11. (*a*) Isosurfaces of instantaneous low-pressure cores showing the vortical structure similar to Robinson (1991), also shown are surface streamlines at the same instant; (*b*) instantaneous azimuthal velocity fluctuations $\overline{v}_\theta'/\omega r$ at $z^+ \approx 5$, contours vary from -0.68 to 0.32, with an increment of 0.04.

has an upward tail preceded by a plateau around 0.75, also similar to the profile near the channel centreline in Kim *et al.* (1987). The location at which sweeps make the same contribution as ejections in the disk flow is higher ($z^+ = 32$) than in the channel ($z^+ = 12$), which is probably due to the difference in Reynolds number between the two flows. Comparison of the contributions from the other two quadrants (first and third) in the disk boundary layer with those from Kim *et al.* (1987) as plotted in the lower half of figure 12 also demonstrates substantial similarities.

In the remainder of this section we shall focus on examining quantitative measures to provide some indirect support to Littell & Eaton's (1994) hypothesis. This is achieved primarily through comparison of two-point spatial correlations in the disk flow with previous measurements in two-dimensional boundary layers. As dis-

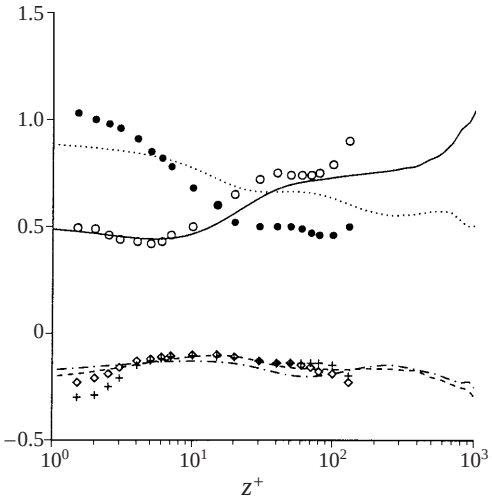

FIGURE 12. Contributions to the primary shear stress from each quadrant normalized by the local mean primary shear stress. Lines: Case 2; symbols: DNS of channel flow (Kim *et al.* 1987); - - - +, first; —— ○, second; –·– ◇, third; ··· ●, fourth quadrant.

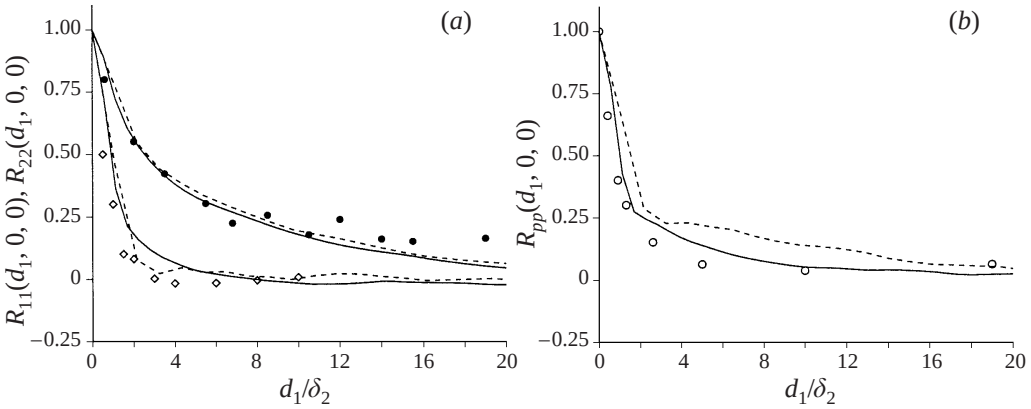

FIGURE 13. (*a*) R_{11} and R_{22} with variable streamwise separation at $z/\delta_2 = 1.4$; (*b*) R_{pp} with variable streamwise separation at the wall; ●, R_{11}, Tritton (1967); ◇, R_{22}, Grant (1958); ○, R_{pp}, Willmarth & Wooldridge (1962); - - -, Case 1; ——, Case 2.

cussed previously, this approach is based on the premise that if two flows contain similar dominant structures, then their two-point correlations will exhibit similar 'signatures' reflected in two-point correlation functions (see Moin & Kim 1985 for further discussion).

A conventional definition of the two-point correlation coefficient is employed (e.g. see Tritton 1967),

$$R_{ij}(d_1, d_2, d_3) = \frac{\langle \overline{v}_i' \overline{v}_j'(d_1, d_2, d_3) \rangle}{\overline{v}_{i,rms}' \overline{v}_{j,rms}'(d_1, d_2, d_3)} \quad (i, j = 1, 2, 3), \tag{4.1}$$

where subscripts 1, 2, and 3 represent streamwise (tangential), wall-normal, and radial directions, respectively. Figure 13(*a*) shows the streamwise two-point correlation coefficients for the tangential and wall-normal fluctuations at $z/\delta_2 = 1.4$.

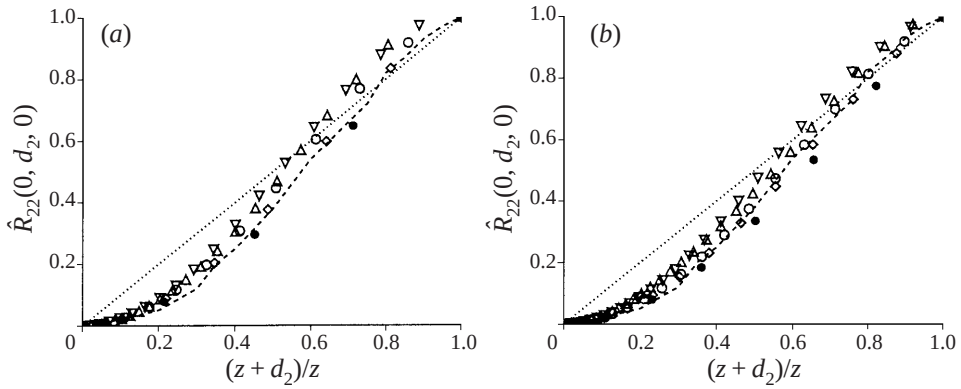

FIGURE 14. Spatial correlation $\widehat{R}_{22}(0, d_2, 0)$ as a function of $(z+d_2)/z$. (*a*) Two-dimensional boundary layer using the method of Lund *et al.* (1998), $Re_{\delta_2} = 2200$; (*b*) Case 2. •, $z^+ = 10$; ◇, $z^+ = 22$; ○, $z^+ = 40$; ∇, $z^+ = 97$; △, $z^+ = 190$; · · ·, Hunt (1984); - - - -, Hunt *et al.* (1989).

Two sets of LES results from Cases 1 and 2 are presented to demonstrate the consistency of the statistics. Also shown are the boundary-layer measurements of Tritton (1967) and Grant (1958). The computed correlation coefficient for the tangential fluctuating velocity $R_{11}(d_1, 0, 0)$ is in good agreement with the measurements of Tritton (1967) and remains positive for a considerable streamwise distance. The correlation coefficient for the wall-normal component $R_{22}(d_1, 0, 0)$ also shows good agreement with Grant (1958). Although the correlation length of $R_{22}(d_1, 0, 0)$ is much smaller than that of $R_{11}(d_1, 0, 0)$, $R_{22}(d_1, 0, 0)$ nevertheless does not take on appreciable negative values which is consistent with the measurements of Townsend (1976) in two-dimensional boundary layers. Figure 13(*b*) compares the wall-pressure correlation coefficient $R_{pp}(d_1, 0, 0)$ with the two-dimensional boundary-layer measurements of Willmarth & Wooldridge (1962). Note R_{pp} is defined similarly as the velocity–velocity correlation R_{ij} in (4.1). As seen in the figure, the wall-pressure correlations exhibit nearly the same characteristics in these two types of flow with rather limited streamwise correlation lengths. The r.m.s. wall-pressure fluctuation used to normalize R_{pp} in the disk flow is $2.5u^{*2}$ (Case 2), compared with $2.54u^{*2}$ quoted in Hinze (1975) for two-dimensional turbulent boundary layers.

Examination of two-point correlations in the context of the structural similarity theory of Hunt *et al.* (1989) is considered in figure 14. As discussed in Hunt *et al.* (1989), the large-scale eddy structure and lengthscales in wall-bounded flows are determined by a combination of shear and blocking. They proposed that the vertical component of the turbulent fluctuations has a self-similar structure in shear boundary layers. Shown in figures 14(*a*) and 14(*b*) are the spatial correlation $\widehat{R}_{22}(0, d_2, 0)$ from LES of a two-dimensional boundary layer using the method of Lund *et al.* (1998) and in the disk flow, respectively. Also shown is the theoretical profile from Hunt (1984) for shear-free boundary layers and the averaged profile of Hunt *et al.* (1989) obtained from previous results in turbulent shear flows. Following Hunt *et al.* (1989), $\widehat{R}_{22}(0, d_2, 0)$ is defined as,

$$\widehat{R}_{22}(0, d_2, 0) = \frac{\langle \overline{v}'_z \overline{v}'_z(0, d_2, 0) \rangle}{\overline{v}'^2_{z,rms}} \quad (d_2 \leqslant 0). \tag{4.2}$$

The similarity between figures 14(*a*) and 14(*b*) is striking. The LES results obtained from both the two-dimensional boundary layer and disk flow exhibit good collapse at

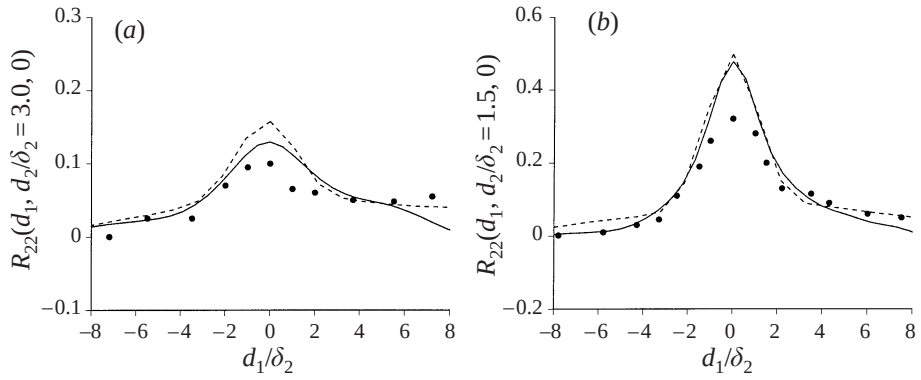

FIGURE 15. R_{22} with fixed wall-normal separation and variable streamwise separation. (*a*) $R_{22}(d_1, d_2/\delta_2 = 3.0, 0)$ at $z/\delta_2 = 1.4$; (*b*) $R_{22}(d_1, d_2/\delta_2 = 1.5, 0)$ at $z/\delta_2 = 2.1$; •, Tritton (1967); - - -, Case 1; ——, Case 2.

different wall-normal locations, indicating strong similarity in $\widehat{R}_{22}(0, d_2, 0)$ with respect to $(z + d_2)/z$. The results are also in good agreement with Hunt *et al.* (1989). In both figures 14(*a*) and 14(*b*), the profiles for $z + d_2 > 0.3z$ can be roughly correlated with a straight line which intersects the abscissa at about $(z + d_2)/z = 0.22$.

Based on the measurements of Grant (1958) and Tritton (1967), Townsend (1976) concluded that except for wall-normal fluctuations, correlations such as R_{12} and R_{11} with constant displacement in the direction of shear, i.e. fixed d_2, and variable displacement in the streamwise direction reach their maximum value for non-zero r_1; $R_{22}(d_1, d_2 = \text{fixed}, 0)$ attains its maximum very close to $d_1 = 0$. The applicability of this observation in the disk flow is examined in the next two figures. Shown in figures 15(*a*) and 15(*b*) are profiles of $R_{22}(d_1, d_2 = 3\delta_2, 0)$ at $z/\delta_2 = 1.4$ and $R_{22}(d_1, d_2 = 1.5\delta_2, 0)$ at $z/\delta_2 = 2.1$, respectively, together with the measurements of Tritton (1967). The specific separation parameters were chosen to match those in Tritton (1967). As in two-dimensional boundary layers, the correlations computed in the disk flow attain their maximum at $d_1 \approx 0$ and there is good overall agreement with the data of Tritton (1967). Note that although the tangential (streamwise) direction in the disk boundary layer is statistically homogeneous, there is nevertheless no *a priori* constraint to require that $R_{22}(d_1, d_2 = \text{fixed}, 0)$ be symmetric with respect to $d_1 = 0$ since a non-zero inhomogeneous dimension d_2 has been introduced into the correlation. Tritton (1967) noted that there is slight asymmetry in the correlation $R_{22}(d_1, d_2 = \text{fixed}, 0)$ with a slower decrease towards zero on the positive d_1 side. The figure shows that this feature seems also to exist in the disk flow.

Figure 16 shows the correlation coefficient $-R_{12}(d_1, d_2 = 3\delta_2, 0)$ at $z/\delta_2 = 1.6$, together with the data of Tritton (1967). The correlation attains a maximum of about 0.14 upstream at separation $d_1 = -1.7\delta_2$ for the disk flow and at $d_1 = -2.0\delta_2$ for the two-dimensional boundary layer. However, the decrease in $-R_{12}(d_1, d_2 = 3\delta_2, 0)$ on the positive d_1 side is much more rapid compared to that of Tritton (1967). The reduced streamwise length scale implied by the more rapid reduction in $-R_{12}(d_1, d_2 = \text{fixed}, 0)$ seems to be consistent with the notion that in 3DTBLs the near-wall shear-producing structures are not quite streamwise but skewed away from the direction of the mean velocity vector as discussed in Johnston & Flack (1996). In general, the results shown in figures 15 and 16 suggest that the observation of Townsend (1976) appears to be applicable to the disk 3DTBL.

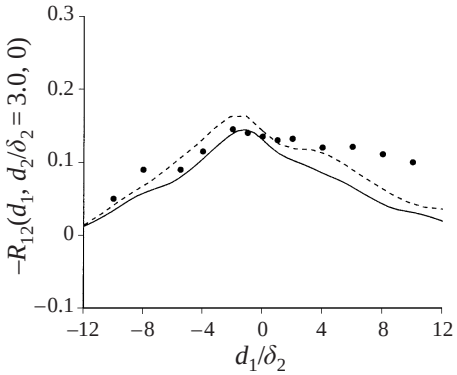

FIGURE 16. $-R_{12}$ with fixed wall-normal separation and variable streamwise separation at $z/\delta_2 = 1.6$. •, Tritton (1967); - - -, Case 1; ——, Case 2.

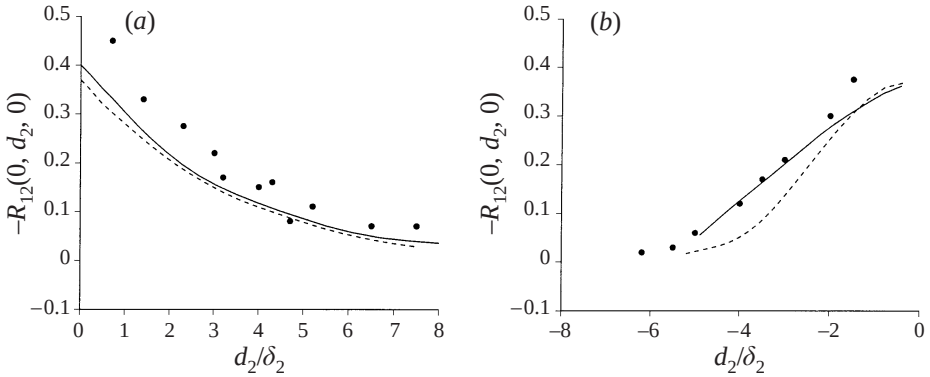

FIGURE 17. $-R_{12}$ with variable wall-normal separation. (*a*) $-R_{12}(0, d_2, 0)$ at $z/\delta_2 = 3.0$; (*b*) $-R_{12}(0, d_2, 0)$ at $z/\delta_2 = 7.0$; •, Tritton (1967); - - -, Case 1; ——, Case 2.

One of the approximate measures for the wall-normal spatial extent of the large eddies responsible for shear stress generation is the correlation coefficient $-R_{12}(0, d_2, 0)$. Shown in figures 17(*a*) and 17(*b*) is $-R_{12}(0, d_2, 0)$ with a positive d_2 separation (away from the disk) starting from $z/\delta_2 = 3$ and $-R_{12}(0, d_2, 0)$ with a negative d_2 separation (towards the disk) starting from $z/\delta_2 = 7$, respectively. Also shown are the measurements of Tritton (1967). Although there are some discrepancies in $-R_{12}(0, d_2, 0)$ between these two types of flow, especially near the zero separation region, the correlations decrease at a similar rate and show fair agreement away from $d_2 = 0$. The limiting value of $-R_{12}(0, d_2 = 0, 0) = 0.4$ obtained from the LES agrees with Littell & Eaton (1994), but is lower than the value of 0.46 quoted in Tritton (1967). Nevertheless, the results shown in figure 17 still indicate it is likely that the wall-normal extent of the large eddies responsible for the generation of the primary shear stress is not substantially different from those in canonical two-dimensional flows.

Further evidence of the structural similarity between these two types of flow can be found in the wall-pressure and velocity correlations. Willmarth & Wooldridge (1962) and Willmarth & Tu (1967) measured spatial correlations between wall-pressure fluctuations and one component of the velocity fluctuations in another point near the wall. One of the important results of their pressure–velocity correlation measurements was that $R_{p2}(d_1, d_2 = \text{fixed}, 0)$ is an odd function of the streamwise

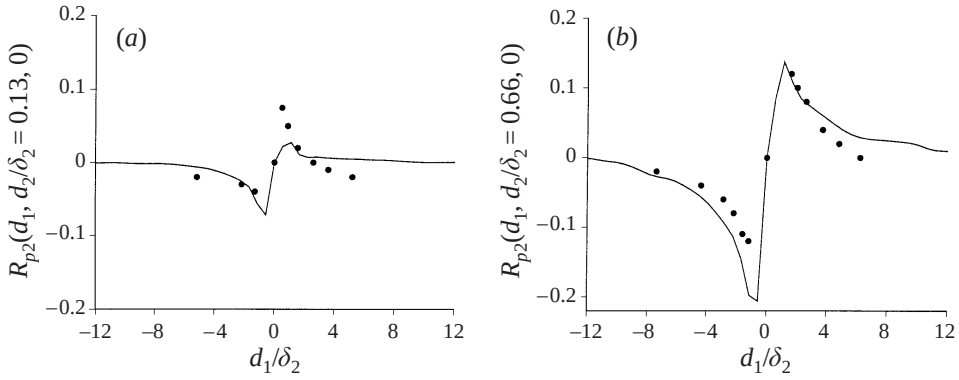

FIGURE 18. Wall-pressure and velocity correlation R_{p2} with fixed wall-normal separation and variable streamwise separation. •, Willmarth & Tu (1967); ——, Case 2.

separation d_1, being positive for $d_1 > 0$ and negative for $d_1 < 0$, consistent with U-shaped vortical structures in the boundary layer (Willmarth & Tu 1967). They also found that for $d_2 > 0.6\delta_2$, the correlation is nearly symmetric with respect to $d_1 = 0$. For planes closer to the wall with small d_2, however, the symmetry was no longer apparent (see also Hinze 1975). Shown in figure 18 is the pressure–velocity correlation $R_{p2}(d_1, d_2 = \text{fixed}, 0)$ in the disk flow, together with the two-dimensional boundary-layer data from Willmarth & Tu (1967). Following Willmarth & Tu (1967), $R_{p2}(d_1, d_2 = \text{fixed}, 0)$ is normalized by the r.m.s. wall pressure fluctuation and the wall-normal fluctuation at $z = 0.66\delta_2$. Profiles of $R_{p2}(d_1, d_2 = 0.13\delta_2, 0)$ and $R_{p2}(d_1, d_2 = 0.66\delta_2, 0)$ are shown in figures 18(*a*) and 18(*b*), respectively. As in two-dimensional turbulent boundary layers, the pressure–velocity correlation $R_{p2}(d_1, d_2 = \text{fixed}, 0)$ is an odd function of the streamwise displacement, taking positive values for $d_1 > 0$ and negative values for $d_1 < 0$. The profile further from the wall shown in figure 18(*b*) has a slightly improved symmetry compared to that closer to the wall shown in figure 18(*a*). For larger streamwise separations $R_{p2}(d_1, d_2 = \text{fixed}, 0)$ decrease rapidly to zero.

The quadrant analysis and two-point correlations in figures 12–18, while not exhaustive, have provided quantitative evidence to support the working hypothesis invoked by Littell & Eaton (1994), i.e. that the overall shear-stress producing structures are similar in the disk 3DTBL and the 2DTBL. Thus, the structural model advanced by Robinson (1991) may be used as a baseline in the disk 3DTBL. A plausible description of the modifications of the baseline model, after taking into account the effect of mean streamwise vorticity, is, in turn, that proposed by Littell & Eaton (1994). The conditionally averaged velocities discussed in connection with figures 9 and 10 obtained from the present LES calculations have offered direct conclusive evidence in support of their proposition.

5. Summary

Large-eddy simulation of the three-dimensional turbulent boundary layer over a rotating disk in an otherwise quiescent incompressible fluid was performed. The boundary layer considered is one of the simplest flows with mean flow three-dimensionality all the way through its laminar origin. It is statistically homogeneous along the streamwise direction and evolves to an equilibrium presumably independent of its initial conditions. A signal-decomposition scheme was developed by modifying

the method of Spalart (1988) and Lund *et al.* (1998) to prescribe time-dependent boundary conditions along the disk radial direction. Entrainment towards the disk surface was prescribed by requiring the mass increment in the radial direction to be balanced with axial entrainment. Predictions from six different parameter cases were presented to study the effects of grid resolution and the SGS model. When the resolution is in a range in which large-scale motions are accurately and well-resolved, the effect of the SGS model and further grid refinement on LES predictions are not significant.

LES predictions show that the skewing angle of the wall shear stress (relative to the disk velocity) is about 16° at a momentum thickness Reynolds number 2660. Compared with the measurements of Littell & Eaton (1994), the maximum errors in the predicted mean tangential and radial velocities using dynamic models are 4% and 2% of the disk speed, respectively. Good agreement was also obtained between the predicted and measured turbulence intensities as well as all three turbulent shear stresses. The one-dimensional spectra of the velocity fluctuations agree reasonably well with the established laws, i.e. -1 slope in the buffer region and $-5/3$ slope near the edge of the boundary layer.

The simulations described in §§ 2 and 3 have answered to a satisfactory degree the call by Johnston & Flack (1996) for turbulence modellers to tackle the disk 3DTBL as a prelude to computation of more complex engineering 3DTBLs. Aside from this, one of the more interesting findings is the conditionally averaged velocities obtained for strong ejection/sweep events. These results have offered new evidence to support the structural model advanced by Littell & Eaton (1994) that streamwise vortices with the same sign as the mean streamwise vorticity are mostly responsible for strong sweep events, streamwise vortices having opposite sign to the mean streamwise vorticity promote strong ejections. Further, two-point velocity–velocity and wall-pressure and velocity correlations exhibit interesting structural similarities with those previously found in two-dimensional turbulent boundary layers. This has provided some quantitative indirect support to the hypothesis invoked by Littell & Eaton (1994) and Johnston & Flack (1996) that appropriate vortical structural models developed for two-dimensional boundary layers (e.g. by Robinson 1991) may be used in equilibrium 3DTBLs. While instructive, future studies directed at understanding the effect of the crossflow on near-wall structures could benefit from consideration of additional techniques used to understand and model coherent motions (e.g. see Jeong *et al.* 1997), possibly using direct simulations. Another area not explored in the current study is evaluation of turbulence models (first- and second-moment closure) against the LES database. Such investigations would seem useful for understanding the strengths and limitations of engineering models used to predict complex boundary layers.

The 3DTBL over a rotating disk considered in this work can be classified as a canonical case, representative of equilibrium 3DTBLs, especially those created over infinite geometries and which are three-dimensional from inception. Examples include the Ekman layer and the 3DTBL created by a rotating free-stream velocity vector (Spalart 1989). Thus, the statistical and structural properties discussed in the present study are expected to apply to other equilibrium 3DTBLs (see also Wu & Squires 1997). However, it should be noted that a straightforward extension of the conclusions drawn from the disk flow to other spatially developing non-equilibrium 3DTBLs, e.g. those over a swept wing, might be too simplistic. Complicating features such as upstream history, streamwise pressure gradient and variation in flow configuration may render the study of these complex spatially developing 3DTBLs a case-by-case endeavour.

This work is supported by the US Office of Naval Research (Grant Numbers N00014-94-1-0047 and N00014-94-1-1053, Program Officer: Dr L. Patrick Purtell and Dr Candace Wark). The authors gratefully acknowledge valuable discussions with Professor J. K. Eaton and Professor T. S. Lund. Most of the simulations were performed on the Cray C90 and T90 at the US Department of Defense High Performance Computing Major Shared Resource Centers (CEWES and NAVO).

REFERENCES

Akselvoll, K. & Moin, P. 1996 Large-eddy simulation of turbulent confined coannular jets. *J. Fluid Mech.* **315**, 387–411.

Anderson, S. D. & Eaton, J. K. 1989 Reynolds stress development in pressure-driven three-dimensional turbulent boundary layers. *J. Fluid Mech.* **202**, 263–294.

Balachandar, S., Streett, C. L. & Malik, M. R. 1992 Secondary instability in rotating disk flow. *J. Fluid Mech.* **242**, 323–347.

Cebeci, T. & Abbott, D. 1975 Boundary layers on a rotating disk. *AIAA J.* **13**, 829–832.

Cham, T. S. & Head, M. R. 1969 Turbulent boundary layer flow on a rotating disk. *J. Fluid Mech.* **37**, 129–147.

Chong, M. S., Soria, J., Perry, A. E., Chacin, J., Na, Y. & Cantwell, B. J. 1996 A study of the turbulence structures of wall-bounded shear flows. *Proceedings of the Summer Program*, Center for Turbulence Research, Stanford University, pp. 383–408.

Coleman, G. N., Ferziger, J. H. & Spalart, P. R. 1990 A numerical study of the turbulent Ekman layer. *J. Fluid Mech.* **213**, 313–348.

Coleman, G. N., Kim, J. & Spalart, P. R. 1996 Direct numerical simulation of strained three-dimensional wall-bounded flows. *Expl Thermal Fluid Sci.* **13**, 239–251.

Copper, P. 1971 Turbulent boundary layer on a rotating disk calculated with an effective viscosity. *AIAA J.* **9**, 255–261.

Ducros, F., Comte, P. & Lesieur, M. 1996 Large eddy simulation of transition to turbulence in a boundary layer developing spatially over a flat plate. *J. Fluid Mech.* **326**, 1–36.

Eaton, J. K. 1995 Effects of mean flow three-dimensionality on turbulent boundary-layer structure. *AIAA J.* **33**, 2020–2025.

Erian, F. F. & Tong, Y. H. 1971 Turbulent flow due to a rotating disk. *Phys. Fluids* **14**, 2588–2591.

Germano, M. 1986 A proposal for a redefinition of the turbulent stresses in the filtered Navier–Stokes equations. *Phys. Fluids* A **29**, 2323–2324.

Germano, M., Piomelli, U., Moin, P. & Cabot, W. H. 1991 A dynamic subgrid-scale eddy viscosity model. *Phys. Fluids* A **3**, 1760–1765.

Grant, H. L. 1958 The large eddies of turbulent motion. *J. Fluid Mech.* **4**, 149–190.

Hinze, J. O. 1975 *Turbulence*, 2nd edn. McGraw-Hill.

Humphrey, J. A. C. & Gor, D. 1993 Experimental observations of an unsteady detached shear layer. *Phys. Fluids* **5**, 2438–2412.

Hunt, J. C. R. 1984 Turbulence structure in thermal convection and shear free boundary layers. *J. Fluid Mech.* **138**, 161–184.

Hunt, J. C. R., Moin, P., Lee, M., Moser, R. D., Spalart, P., Mansour, N. N., Kaimal, J. C. & Gaynor, E. 1989 Cross correlation and length scales in turbulent flows near surfaces. In *Advances in Turbulence*, vol. 2, pp. 128–134. Springer.

Jeong, J., Hussian, F., Schoppa, W. & Kim, J. 1997 Coherent structures near the wall of turbulent channel flow. *J. Fluid Mech.* **332**, 185–214.

Johnston, J. P. & Flack, K. A. 1996 Review – Advances in three-dimensional turbulent boundary layers with emphasis on the wall-layer regions. *J. Fluids Engng* **118**, 219–232.

Kang, H. S., Choi, H. & Yoo, J. Y. 1998 On the modification of the near-wall coherent structure in a three-dimensional turbulent boundary layer on a free rotating disk. *Phys. Fluids* **10**, 2315–2322.

Kim, J. & Moin, P. 1986 The structure of the vorticity field in turbulent channel flow. Part 2. Study of ensemble-averaged fields. *J. Fluid Mech.* **162**, 339–363.

Kim, J., Moin, P. & Moser, R. 1987 Turbulence statistics in fully developed channel flow at low Reynolds number. *J. Fluid Mech.* **177**, 133–166.

Kobayashi, R. 1994 Review: laminar-to-turbulent transition of three-dimensional boundary layers on rotating bodies. *J. Fluids Engng* **116**, 200–211.

Kravchenko, A. G. & Moin, P. 1997 On the effect of numerical errors in large eddy simulations of turbulent flows. *J. Comput. Phys.* **131**, 310–322.

Lesieur, M. & Metais, O. 1996 New trends in large-eddy simulation of turbulence. *Ann. Rev. Fluid Mech.* **28**, 45–82.

Lingwood, R. L. 1996 An experimental study of absolute instability of the rotating disk boundary layer flow. *J. Fluid Mech.* **314**, 373–405.

Lingwood, R. L. 1997 On the effects of suction and injection on the absolute instability of the rotating disk boundary layer flow. *Phys. Fluids* **9**, 1317–1328.

Littell, H. S. & Eaton, J. K. 1994 Turbulence characteristics of the boundary layer on a rotating disk. *J. Fluid Mech.* **266**, 175–207.

Lund, T. S., Wu, X. & Squires, K. D. 1998 Generation of turbulent inflow data for spatially-developing boundary layer simulations. *J. Comput. Phys.* **140**, 233–258.

Malik, M. R., Wilkinson, S. P. & Orszag, S. A. 1981 Instability and transition in rotating disk flow. *AIAA J.* **19**, 1131–1138.

Mittal, R. & Moin, P. 1997 Suitability of upwind-biased finite difference schemes for large eddy simulation of turbulent flows. *AIAA J.* **35**, 1415–1417.

Moin, P. & Kim, J. 1985 The structure of the vorticity field in turbulent channel flow. Part 1. Analysis of instantaneous files and statistical correlations. *J. Fluid Mech.* **155**, 441–464.

Moin, P., Shih, T. H., Driver, D. & Mansour, N. N. 1990 Direct numerical simulation of a three-dimensional turbulent boundary layer. *Phys. Fluids* A **2**, 1846–1853.

Perry, A. E., Henbest, S. M. & Chong, M. S. 1986 A theoretical and experimental study of wall turbulence. *J. Fluid Mech.* **165**, 163–199.

Rai, M. M. & Moin, P. 1993 Direct numerical simulation of transition and turbulence in a spatially evolving boundary layer. *J. Comput. Phys.* **109**, 169–192.

Robinson, S. K. 1991 Coherent motions in the turbulent boundary layer. *Ann. Rev. Fluid Mech.* **23**, 601–639.

Rodi, W., Ferziger, J. H., Breuer, M. & Pourquie, M. 1997 Status of large eddy simulation: results of a workshop. *J. Fluids Engng* **119**, 248–262.

Schlichting, H. 1979 *Boundary Layer Theory*, 7th edn. McGraw-Hill.

Schwarz, W. R. & Bradshaw, P. 1994 Turbulence structural changes for a three-dimensional turbulent boundary layer in a 30° bend. *J. Fluid Mech.* **272**, 183–209.

Scotti, A., Meneveau, C. & Lilly, D. K. 1993 Generalized Smagorinsky model for anisotropic grids. *Phys. Fluids* A **5**, 2306–2308.

Sendstad, O. & Moin, P. 1992 The near wall mechanics of three-dimensional turbulent boundary layers. *Report TF-57*, Mechanical Engineering Department, Stanford University.

Simpson, R. L. & Olcmen, S. M. 1995 An experimental study of a three-dimensional pressure-driven turbulent boundary layer. *J. Fluid Mech.* **290**, 225–262.

Spalart, P. R. 1988 Direct simulation of a turbulent boundary layer up to $Re_\theta = 1410$. *J. Fluid Mech.* **187**, 61–98.

Spalart, P. R. 1989 Theoretical and numerical study of a three-dimensional turbulent boundary layer. *J. Fluid Mech.* **205**, 319–340.

Townsend, A. A. 1976 *The Structure of Turbulent Shear Flow*, 2nd edn. Cambridge University Press.

Tritton, D. J. 1967 Some new correlation measurements in a turbulent boundary layer. *J. Fluid Mech.* **28**, 439–462.

Vasilyev, O. V., Lund, T. S. & Moin, P. 1998 A general class of commutative filters for LES in complex geometries. *J. Comput. Phys.* **146**, 105–123.

Vreman, B., Geurts, B. & Kuerten, H. 1994 On the formulation of the dynamic mixed subgrid-scale model. *Phys. Fluids* **6**, 4057–4059.

Vreman, B., Geurts, B. & Kuerten, H. 1997 Large eddy simulation of the turbulent mixing layer. *J. Fluid Mech.* **339**, 357–390.

Wang, M. & Moin, P. 1997 Large eddy simulation of trailing-edge turbulence and aeroacoustics. *Bull. Am. Phys. Soc.* **42**, 2137.

Webster, D., Degraaff, D. & Eaton, J. K. 1996 Turbulence characteristics of a boundary layer over a swept bump. *J. Fluid Mech.* **323**, 1–22.

Willmarth, W. W. & Tu, B. J. 1967 Structure of turbulence in the boundary layer near the wall. *Phys. Fluids Suppl.* S134–S137.

Willmarth, W. W. & Wooldridge, C. E. 1962 Measurements of the fluctuating pressure at the wall beneath a thick turbulent boundary layer. *J. Fluid Mech.* **14**, 187–210.

Wu, X. & Squires, K. D. 1997 Large eddy simulation of an equilibrium three-dimensional turbulent boundary layer. *AIAA J.* **35**, 67–74.

Wu, X. & Squires, K. D. 1998*a* Numerical investigation of the turbulent boundary layer over a bump. *J. Fluid Mech.* **362**, 229–271.

Wu, X. & Squires, K. D. 1998*b* Predictions of the three-dimensional turbulent boundary layer over a swept bump. *AIAA J.* **36**, 505–514.

Wu, X. & Squires, K. D. 1998*c* Predictions of the high Reynolds number flow over a two-dimensional bump. *AIAA J.* **36**, 799–808.

Zang, Y., Street, R. & Koseff, J. R. 1993 A dynamic mixed subgrid-scale model and its application to turbulent recirculating flows. *Phys. Fluids* **5**, 3186–3196.